



AIAA 99-1006

High-Resolution Genuinely Multidimensional  
Solution of Conservation Laws by the  
Space-Time Conservation Element and  
Solution Element Method

Ananda Himansu<sup>1</sup>, Sin-Chung Chang<sup>2</sup>, Sheng-Tao Yu<sup>3</sup>,  
Xiao-Yen Wang<sup>1</sup>, Ching-Yuen Loh<sup>1</sup>  
and Philip C.E. Jorgenson<sup>2</sup>

<sup>1</sup> Taitech Inc., NASA Lewis, Cleveland, OH

<sup>2</sup> NASA Lewis Research Center, Cleveland, OH

<sup>3</sup> Wayne State University, Detroit, MI

This is a preprint or reprint of a paper intended for presentation at a conference. Because changes may be made before formal publication, this is made available with the understanding that it will not be cited or reproduced without the permission of the author.

**37th AIAA Aerospace Sciences  
Meeting and Exhibit**  
**January 11-14, 1999 / Reno, NV**



# High-Resolution Genuinely Multidimensional Solution of Conservation Laws by the Space-Time Conservation Element and Solution Element Method

Ananda Himansu\*    Sin-Chung Chang†    Sheng-Tao Yu‡    Xiao-Yen Wang§  
Ching-Yuen Loh¶    Philip C.E. Jorgenson||

## Abstract

In this overview paper, we review the basic principles of the method of space-time conservation element and solution element for solving the conservation laws in one and two spatial dimensions. The present method is developed on the basis of local and global flux conservation in a space-time domain, in which space and time are treated in a unified manner. In contrast to the modern upwind schemes, the approach here does not use the Riemann solver and the reconstruction procedure as the building blocks. The drawbacks of the upwind approach, such as the difficulty of rationally extending the 1D scalar approach to systems of equations and particularly to multiple dimensions is here contrasted with the uniformity and ease of generalization of the CE/SE 1D scalar schemes to systems of equations and to multiple spatial dimensions. The assured compatibility with the simplest type of unstructured meshes, and the uniquely simple nonreflecting boundary conditions of the present method are also discussed. The present approach has yielded high-resolution shocks, rarefaction waves, acoustic waves, vortices, ZND detonation waves and shock/acoustic waves/vortices interactions. Moreover, since no directional splitting is employed, numerical resolution of two-dimensional calculations is comparable to

that of the one-dimensional calculations. Some sample applications displaying the strengths and broad applicability of the CE/SE method are reviewed.

## 1 Introduction

This paper provides an introductory overview of a new numerical framework for solving conservation laws, namely, the Method of Space-Time Conservation Element and Solution Element, or the CE/SE method for short. The method has been developed in the past few years by Chang and coworkers [1-31]. This method was designed from scratch to be a coherent framework, and is not an incremental improvement of a previously existing method. All the numerical schemes obtained by application of this method share the attributes of generality, accuracy and simplicity. The method has been applied by Chang and coworkers to obtain numerical schemes for conservation laws in fluid dynamics. However, the method could also be applied to other continuum conservation laws, such as those encountered in electromagnetics.

\*Taitech, Inc., NASA Lewis Res. Center

†NASA Lewis Res. Center, Cleveland, OH 44135

‡Dept. of Mechanical Engr., Wayne State Univ.

§Taitech, Inc., NASA Lewis Res. Center

¶Taitech, Inc., NASA Lewis Res. Center

||NASA Lewis Res. Center, Cleveland, OH 44135

Copyright ©1998 American Institute of Aeronautics and Astronautics, Inc. No copyright is asserted in the United States under Title 17, U.S. Code. The U.S. Government has a royalty-free license to exercise all rights under the copyright claimed herein for Governmental Purposes. All other rights are reserved by the copyright owner.

The CE/SE method is distinguished from other methods by its very conceptual basis — flux conservation in space-time. The original reports described the present method in a thorough and highly detailed fashion. That is, starting from the basic integral equations, the algebraic details of the discretization and the stability and error analyses were presented in a systematic way. One of the aims of this overview is to provide the reader unfamiliar with the CE/SE method with a gentler introduction to the method. In this overview, following the treatment of

[11], the CE/SE method is described in a more intuitive manner by focusing on the geometric nature of its unique space-time discretization. This will give the reader a complete and simple conceptual description of CE/SE algorithms in one and more spatial dimensions. For algebraic details of the schemes and numerical analysis of their properties, the reader is referred to the original papers. The geometric description clarifies the conceptual and algorithmic differences between the CE/SE method and traditional numerical methods for conservation laws. This highlighting of these differences is another aim of the current paper. The third aim of this paper is to review some sample numerical results obtained with CE/SE schemes, in order to give the reader some indication of the accuracy and broad applicability demonstrated already by the method. A fourth aim is to provide the reader with a CE/SE bibliography, complete as of July 1998.

To persuade the reader of the advantages of the CE/SE approach, the key features and principal successes of the method will now be briefly listed. The statements will be supported by the exposition in later sections of the paper. Some distinguishing features of the CE/SE method are : (i) Although the differential form is also utilized, the main emphasis of the present method is on solving the integral form of the conservation equations in the space-time domain. (ii) The conservation laws are recognized as balances of space-time fluxes exiting space-time regions. The present method was therefore designed to conserve space-time flux locally and globally. Conventional ‘conservative’ schemes, however, calculate spatial fluxes at an instant of time; they do not recognize the importance of conservative treatment of the temporal evolution. The space-time flux perspective allows for truly conservative treatment of moving boundaries and moving meshes. (iii) The discretized equations obtained by the present method are a faithful discrete counterpart of the conservation laws, automatically reproducing the key properties of the latter, such as characteristics-related properties. For example, for isentropic flows, the present method can be used to construct explicit solvers that are non-dissipative (neutrally stable) for all Courant numbers  $\leq 1$ . Also, these solvers are two-way time-marching schemes, i.e., each forward-time-marching scheme can be inverted to become a backward-time-marching scheme, which is also neutrally stable. In other words, the marching variables at the  $(n-1)$ th time level can be determined in terms of those at the  $n$ th time level. Thus, these solvers reproduce the time-reversibility displayed by isen-

tropic initial-value flow problems arising from pure convection phenomena. (iv) A staggered space-time mesh is used, i.e., the spatial arrangement of the mesh nodes at any time level is spatially staggered relative to the arrangement at the previous time level. This ensures that flow information at each interface separating two conservation elements can be evaluated without interpolation (e.g., averaging) or extrapolation. In particular, no Riemann solver is needed in calculating interfacial fluxes. (v) The flow solution structure is not calculated through a reconstruction procedure. Instead, the gradients of flow variables are treated as independent unknowns, and they are not influenced by the flow properties in neighboring elements at the same time level. This is in full compliance with the flow physics of the initial-value problem. (vi) For flows in multiple spatial dimensions, no directional splitting is employed. The two and three-dimensional spatial meshes employed by the present method are built from triangles and tetrahedrons, respectively. The CE/SE schemes in two and three spatial dimensions are naturally formulated on unstructured triangular and tetrahedral meshes which are the most easily generated meshes for complicated flow boundary geometries. (vii) The explicit time-marching CE/SE algorithms for initial-value and initial-boundary-value problems are easy to vectorize and parallelize, in order to take advantage of advanced computer architectures. (viii) The flux-based specification of the CE/SE schemes give rise in a natural fashion to extremely simple yet highly effective non-reflecting boundary conditions. This is in contrast to the complexity of non-reflecting boundary conditions necessary for traditional numerical methods.

Computer programs based on the CE/SE method have been developed for calculating flows in one and two spatial dimensions. Numerous results were obtained [1-31], including various shock tube problems, the ZND detonation waves, the implosion and explosion problem, shocks over a forward-facing step, acoustic waves, and shock/acoustic wave interactions. The method can clearly resolve shock/acoustic wave interactions wherein the difference of the magnitude between acoustic wave and shock could be up to six orders. In two-dimensional flows, the reflected shock is as crisp as the leading shock. From the evidence of these results, the CE/SE method has proved to be a promising numerical framework for solving fluid dynamics problems.

The remainder of the paper is organized as follows. In Sec. 2, we contrast the present perspective

of conservation of space-time fluxes with the traditional focus on conservation of spatial fluxes. A new space-time integral form of conservation laws will be described. In Sec. 3, we present the CE/SE method for solving flow equations in one spatial dimension. In Secs. 4 and 5, the extensions of the CE/SE method in two and three spatial dimensions, without directional-splitting, are illustrated. In Sec. 6, numerical examples calculated by the present method are shown. Sec. 7 has a summary and concluding remarks.

## 2 Numerical Methods from the Space-Time Perspective

### 2.1 Finite-Volume Conservative Discretization

The finite-volume method is the traditional numerical method that is conceptually closest to the present method. Therefore, we begin this section with some remarks regarding the basis and limitations of upwind finite volume discretizations. Historically, the solution of conservation laws was first viewed as being reducible to the solution of ordinary or partial differential equations, with specified initial and boundary conditions. As the development of numerical methods for differential equations matured, it was recognized that flux-conservative numerical schemes were essential for the accurate computation of flowfields with shocks and other embedded discontinuities. This property of conservative differencing was due to its mimicking of integral flux balances, which are applicable to discontinuities. With the early emphasis on steady state solutions, the conventional finite volume methods for simulating conservation laws were focused on spatial flux balance over a *fixed spatial domain*. Modern upwind techniques that stem from Godunov's scheme, and which follow the projection-upwinding-evolution framework described by van Leer [39, 40]. A particularly lucid description of the modern upwind approach is found in Huynh [41].

Consider conservation of any extensive property with continuum distribution per unit volume  $u$ , and spatial flux vector  $\vec{f}$ . The differential form of the conservation or transport law, which applies in the absence of discontinuities of the solution and its gra-

dient, is

$$\frac{\partial u}{\partial t} = -\nabla \cdot \vec{f}, \quad (2.1)$$

where  $\nabla$  is the spatial gradient operator. It is this differential form that is numerically approximated by finite-difference techniques. Integrating Eq. (2.1) over a fixed spatial volume  $V$ , and using Gauss' divergence theorem to convert the volume integral on the right-hand-side to a surface integral, we obtain

$$\frac{d}{dt} \int_V u dV = - \int_{S(V)} \vec{f} \cdot d\vec{S}, \quad (2.2)$$

where  $S(V)$  is the boundary of  $V$ , and  $d\vec{S} = d\sigma \vec{n}$  with  $d\sigma$  and  $\vec{n}$ , respectively, being the area and the outward unit normal vector of a surface element on  $S(V)$ . Eq. (2.2) is the balance at a particular instant of time between the spatial fluxes exiting a finite spatial volume, and the time rate of change of a quantity within the volume. The traditional finite volume methods concentrate on the conservative evaluation of the right hand side of Eq. (2.2). The left hand side of Eq. (2.2) is often discretized by a finite difference method, such as the Runge Kutta method. Thus, while the spatial fluxes are treated in an integral sense, the flux of the solution in the time direction is still treated in a differential manner. This means that the balancing of fluxes occurs only at discrete instants of time. The solution in between these instants will not in general display exact balance of the numerical fluxes. This allows the numerical solution to "leak away" as it evolves in time. Thus energy and other quantities will generally not be globally conserved in an evolving unsteady flow.

If we integrate Eq. (2.2) with respect to time, we obtain

$$\int_V u dV \Big|_{t_1}^{t_2} = - \int_{t_1}^{t_2} dt \int_{S(V)} \vec{f} \cdot d\vec{s}. \quad (2.3)$$

Note that Eq. (2.3) is more fundamental than Eq. (2.1), and applies even to discontinuous solutions such as shock waves and contact discontinuities. For smooth solutions, Eq. (2.1) can be obtained from Eq. (2.3) by application of Gauss' divergence theorem to arbitrary volumes. Eq. (2.3) is indeed an integral form of the flux balances, and it is the starting point for some finite-volume discretizations. However, even this form has a drawback, namely, that the spatial volume  $V$  is unchanging in time. This fact, coupled with a spatial (rather than space-time) perspective on flux conservation, means that in the finite-volume context, Eq. (2.3) is generally applied to a spatial mesh that is the same at successive time

levels. The same kind of mesh is used also when the left-hand side of Eq. (2.2) is treated by Runge-Kutta integration, or other such method. This awkward space-time mesh arrangement evolved from the limited viewpoint of considering conservation of only the spatial fluxes. As will be shown next, it leads to the necessity of averaging fluxes at interfaces between cells, which is in turn the source of much complexity and difficulty.

As shown in Fig. 2.1(a), due to the fixed spatial domain assumed in Eq. (2.3), the shape of the space-time Conservation Elements (CEs) in one spatial dimension must be rectangular. In addition, because of the limited spatial perspective of the mesh in most discretizations, these elements are generally stacked exactly on top of each other in the time direction, i.e., no staggering of these elements in time is used. If Eq. (2.2) is used instead, the spatial CEs are just the horizontal line segments in Fig. 2.1(a). For equations in two spatial dimensions, as depicted in Fig. 2.1(b), a conservation element is a uniform-cross-section cylinder in space-time, and again no staggering in time is employed. This arrangement results in vertical interfaces extended in the direction of time evolution between adjacent CEs. Across these interfaces, flow property information from the previous time level travels in both directions. Therefore, in calculating the interfacial flux which is needed to balance fluxes for the CEs, two values of the interfacial flux are obtained, one from each of the two CEs which share the interface. To reconcile these two values and obtain a unique value of the interfacial flux, some form of averaging becomes necessary. A simple arithmetic averaging of fluxes leads to a central-difference approximation of the spatial derivatives. In modern high-resolution schemes, to better model the flow of information, the averaging is accomplished by upwind biasing (or a Riemann solver). However, this upwind biasing, termed flux-splitting for systems of equations, is based on the Method of Characteristics, which is valid only for smooth solutions and does not apply to solution discontinuities such as shocks. Further, for flows in multiple spatial dimensions, directional splitting is used to implement one-dimensional characteristic flux splitting. This practice causes deterioration of numerical resolution and difficulties in solving conservation laws with source terms, because source terms have no preferred direction.

We mention here that besides the need for the averaging of fluxes at interfaces, there are other sources of complexity and difficulty in the conven-

tional finite-volume approach. One such source is that typically the unknowns in the discretized solution are just the values of the solution at the mesh points. At any mesh point, the numerical approximations to the flow gradients, which are needed for higher accuracy, must be recovered using the discretized solution at the mesh point and the neighboring mesh points. This procedure is termed projection or reconstruction, and is normally accomplished by fitting a polynomial to the solution at neighboring mesh points. In the vicinity of shocks, however, this results in spatial oscillations in the solution. This problem is addressed through the use of complex flux-limiting strategies, such as Total Variation Diminishing and Essentially Non-Oscillatory schemes, etc., which use some non-general properties of simple shock waves.

Schemes that use a staggered space-time mesh, of course, date back to such classical schemes as the Leapfrog scheme, which latter scheme in actuality computes two decoupled staggered-mesh solutions. In general, they are not currently favored by the CFD community. However, we point out that there are some staggered space-time mesh schemes developed prior to the current work, which continue to be researched. Sanders [47] and Sanders and Weiser ([48], [49]) developed a staggered mesh scheme. However, they did not gain the potential benefit of avoiding upwinding, because they used the method of characteristics as part of their solution procedure. Nessyahu and Tadmor [46] also developed a staggered mesh scheme. However, they did not treat the flow gradients as independent unknowns at the mesh point, and were thus led to reconstructive procedures. Both the preceding schemes are dissipative and therefore irreversible. The present method was developed independently in a different framework by Chang and coworkers, without knowledge of the schemes of Sanders and Weiser, or of Nessyahu and Tadmor.

## 2.2 Space-Time Integral Form of the Governing Equations

We now present the space-time integral form of the governing equations that is the starting point for the CE/SE method. For ease of exposition, we will deal with the one-dimensional Euler equations. The one-dimensional unsteady Euler equations of a perfect gas can be expressed as

$$\mathbf{U}_t + \mathbf{F}_x = \mathbf{0}, \quad (2.4)$$

where

$$\mathbf{U} = \begin{pmatrix} u_1 \\ u_2 \\ u_3 \end{pmatrix} = \begin{pmatrix} \rho \\ \rho v \\ \rho E \end{pmatrix}, \quad (2.5)$$

$$\mathbf{F} = \begin{pmatrix} f_1 \\ f_2 \\ f_3 \end{pmatrix} = \begin{pmatrix} \rho v \\ \rho v^2 + p \\ (\rho E + p)v \end{pmatrix}, \quad (2.6)$$

with  $\rho$ ,  $v$ ,  $p$ , and  $E$  being the density, velocity, static pressure, and specific total energy, respectively. By definition,  $E = v^2/2 + e$ , where  $e$  is the specific internal energy. The equation of state is  $p = (\gamma - 1)\rho e$  with  $\gamma$  being the specific heat ratio.

As shown in Fig. 2.2, let  $x_1 = x$ , and  $x_2 = t$  be the coordinates of a two-dimensional Euclidean space  $E_2$ . Then Eq. (2.4) can be expressed as the divergence-free conditions

$$\nabla \cdot \vec{h}_m = 0, \quad m = 1, 2, 3, \quad (2.7)$$

where  $\nabla$  here denotes the space-time gradient operator  $(\partial/\partial x, \partial/\partial t)$ , and  $\vec{h}_m = (f_m, u_m)$ ,  $m = 1, 2, 3$ , are the *space-time* mass, momentum, and energy current-density vectors, respectively. Equation (2.7) is valid everywhere in  $E_2$  for continuous and isentropic flow solutions. For flows with shock waves, we must use the more fundamental form of the conservation laws:

$$\oint_{S(R)} \vec{h}_m \cdot d\vec{s} = 0, \quad m = 1, 2, 3. \quad (2.8)$$

Here  $S(R)$  is the boundary of a space-time region  $R$ , and  $d\vec{s} = d\sigma \vec{n}$  with  $d\sigma$  and  $\vec{n}$ , respectively, being the area and the outward unit normal vector of a surface element on  $S(R)$ . Note that (i) because  $\vec{h}_m \cdot d\vec{s}$  is the space-time flux of  $\vec{h}_m$  leaving  $R$  through  $d\vec{s}$ , Eq. (2.8) simply states that the total space-time flux of  $\vec{h}_m$  leaving  $R$  through its boundary vanishes; (ii) all mathematical operations can be carried out as though  $E_2$  were an ordinary two-dimensional Euclidean space; and (iii) Eq. (2.7) is valid only for smooth flows, and it can be derived from Eq. (2.8) using Gauss' divergence theorem. Since it places no constraint on the shape of the CEs in the space-time domain, Eq. (2.8) is more general than the usual mathematical statement of a conservation law, as typified by Eq. (2.2) or Eq. (2.3). Eq. (2.8) is the space-time integral form that is numerically approximated in the CE/SE method. For the CEs as defined in CE/SE schemes to date, Eq. (2.3) suffices. However, an alternate derivation of 1D CE/SE schemes requires the use of Eq. (2.8). The form Eq. (2.8) is also essential for the oblique cylinder CEs that will

arise when the CE/SE method is applied to moving boundary or moving mesh problems. Also, the space-time perspective inherent in Eq. (2.8) frees up the researcher to visualize spatial meshes that are not stacked directly one on top of another in the time direction, but are instead spatially staggered relative to previous time levels.

### 2.3 An Ideal Numerical Analogue

A smooth solution to the Euler equations, Eq. (2.4), has the following important properties: (i) it does not dissipate with time; (ii) its value at any point  $(x, t)$  has a finite domain of dependence at an earlier time; and (iii) it is completely determined by the initial data at a given time. In the light of these properties, we remark that (i) a solution to a dissipative numerical scheme will dissipate with time; (ii) the value of a solution to an implicit scheme at any point  $(x, t)$  depends on all the initial data and all the boundary data up to the time  $t$ ; and (iii) a scheme involving more than two time levels requires the specification of the initial data at more than one time level. Therefore, we conclude that an ideal numerical analogue to Eq. (2.4) should be *neutrally stable*, *explicit*, and involving only *two time levels*.

By adding an artificial dissipation term to introduce irreversibility, an ideal solver of Eq. (2.4) can be extended to model flows with shocks. We want to emphasize that the artificial dissipation in an ideal numerical method should occur only in shock capturing; without added artificial damping, there should be no other source of numerical dissipation.

Furthermore, in an ideal Navier Stokes solver, the above guidelines of modeling the Euler equations should be applied to the discretization of the convective terms of the Navier Stokes equations. We note that, stripped of any added artificial terms, traditional numerical schemes are in general not free from inherent numerical dissipation. For flows at large Reynolds numbers, numerical dissipation may overwhelm the physical dissipation and cause a complete distortion of the solution. Because an ideal analogue of Eq. (2.4) has no numerical dissipation, when it is applied to discretize the convective terms of the Navier Stokes equations, the Navier-Stokes solver has the property that the numerical dissipation of its solutions approaches zero as the physical dissipation approaches zero.

### 3 The CE/SE Method in One Spatial Dimension

By comparison with modern upwind finite-volume methods for hyperbolic equations, the following distinguishing features of the CE/SE method result in a simpler and more consistent numerical flow model: (i) A space-time discretization is chosen for the flux conservation such that there is no Riemann problem to be solved at the cell interface. (ii) To avoid imposing predetermined constraints on the flow solutions such as monotonicity and TVD, the flow properties and their gradients are treated as unknowns. For smooth flows, the unknowns are completely determined by flux conservation, and the resultant numerical procedure can march forward and backward in time. (iii) For flows with shocks, an adjustable artificial damping is added to the discretized equations such that the numerical entropy condition is satisfied.

#### 3.1 Preliminaries

For simplicity, we develop the CE/SE Euler solver on a uniform staggered space-time mesh. In Fig. 3.1, we illustrate the nodes, denoted by dots (filled circles), where the unknowns are located. The space and time intervals between neighboring nodal lines are respectively denoted by  $\Delta x/2$  and  $\Delta t/2$ . Note that the spatial interval between nodes at a given time level is denoted by  $\Delta x$ . The reason for the notation  $\Delta t/2$  for the interval between successive time levels is to emphasize that on this staggered space-time mesh, it takes two half-time-steps to return to the original spatial node locations. There is a Solution Element (SE) associated with each node  $(j, n)$ . Let the  $SE(j, n)$  be the interior of the space-time region bounded by a dashed line depicted in Fig. 3.2. It includes a horizontal line segment, a vertical line segment, and their immediate neighborhood. Between SEs, discontinuities are allowed. For the Euler equations, Eq. (2.4), which have no source terms, the actual size of the neighborhood does not matter.

Within a SE, the flow property vector  $\mathbf{U}$  and the flux vector  $\mathbf{F}$  are approximated by their discretized counterparts  $\mathbf{U}^*$  and  $\mathbf{F}^*$ . Since a second-order scheme is desired, piecewise linear functions of space and time  $\mathbf{U}^*$  and  $\mathbf{F}^*$  are assumed. For  $(x, t)$  in  $SE(j, n)$ , we assume that

$$\mathbf{U}^*(x, t; j, n) =$$

$$\mathbf{U}_j^n + (\mathbf{U}_x)_j^n (x - x_j) + (\mathbf{U}_t)_j^n (t - t^n) \quad (3.1)$$

and

$$\begin{aligned} \mathbf{F}^*(x, t; j, n) = \\ (\mathbf{F})_j^n + (\mathbf{F}_x)_j^n (x - x_j) + (\mathbf{F}_t)_j^n (t - t^n). \end{aligned} \quad (3.2)$$

This is the Taylor polynomial of degree one within each element, and the expansion coefficients  $\mathbf{U}_j^n$ , etc., are the column matrices of unknown constants to be determined for each  $SE(j, n)$ .  $\mathbf{F}_j^n$  is the column matrix  $\mathbf{F}$  (which is a function of  $\mathbf{U}$ ) evaluated with  $\mathbf{U} = \mathbf{U}_j^n$ .

The expansion coefficients  $(\mathbf{U}_t)_j^n$ ,  $(\mathbf{F}_x)_j^n$  and  $(\mathbf{F}_t)_j^n$  in Eqs. (3.1) and (3.2) will be expressed as functions of the independent unknowns  $\mathbf{U}_j^n$  and  $(\mathbf{U}_x)_j^n$  of the present scheme as follows:

$$(\mathbf{F}_x)_j^n = \mathbf{A}_j^n (\mathbf{U}_x)_j^n, \quad (3.3)$$

$$(\mathbf{U}_t)_j^n = -(\mathbf{F}_x)_j^n, \quad (3.4)$$

and

$$(\mathbf{F}_t)_j^n = \mathbf{A}_j^n (\mathbf{U}_t)_j^n. \quad (3.5)$$

Here (i)  $\mathbf{A}_j^n$  is the Jacobian matrix  $\mathbf{A} = \partial \mathbf{F} / \partial \mathbf{U}$  (which is a function of  $\mathbf{U}$ ) evaluated with  $\mathbf{U} = \mathbf{U}_j^n$ , and (ii) Eqs. (3.3), (3.5) and (3.4) are the numerical analogues of the chain-rule relations  $\mathbf{F}_x = \mathbf{A} \mathbf{U}_x$ ,  $\mathbf{F}_t = \mathbf{A} \mathbf{U}_t$  and the differential equation, Eq. (2.4), respectively. Furthermore, because the space-time flux vectors  $\tilde{\mathbf{h}}_m = (f_m, u_m)$ ,  $m = 1, 2, 3$ , we shall assume that for  $m = 1, 2, 3$ ,

$$\tilde{\mathbf{h}}_m^*(x, t; j, n) = (f_m^*(x, t; j, n), u_m^*(x, t; j, n)), \quad (3.6)$$

where  $u_m^*$  and  $f_m^*$ ,  $m = 1, 2, 3$ , are the components of the column matrices  $\mathbf{U}^*$  and  $\mathbf{F}^*$ , respectively.

At this juncture, note that hereafter, the components of the column matrices  $\mathbf{U}_j^n$ ,  $(\mathbf{U}_x)_j^n$ ,  $(\mathbf{U}_t)_j^n$ ,  $\mathbf{F}_j^n$ ,  $(\mathbf{F}_x)_j^n$  and  $(\mathbf{F}_t)_j^n$ , will be denoted by  $(u_m)_j^n$ ,  $(u_{mx})_j^n$ ,  $(u_{mt})_j^n$ ,  $(f_m)_j^n$ ,  $(f_{mx})_j^n$  and  $(f_{mt})_j^n$ ,  $m = 1, 2, 3$ , respectively.

#### 3.2 Discretization of Space-Time Conservation Laws

For smooth flows, the calculations of  $\mathbf{U}_j^n$  and  $(\mathbf{U}_x)_j^n$  are determined by requiring fluxes to be conserved over space-time Conservation Elements (CEs). As depicted in Figs. 3.3(a) and 3.3(b), two CEs, denoted by  $CE_-(j, n)$  and  $CE_+(j, n)$ , are associated with every mesh point  $(j, n)$ . A glance over Figs. 3.1,

3.2, and 3.3 reveals that the set of  $\text{CE}_{\pm}(j, n)$  over all mesh points  $(j, n)$  do not overlap among themselves and can fill the entire space-time computational domain.

For each  $(j, n)$ , the following discrete analogues to the space-time flux conservation, Eq. (2.8), are imposed:

$$\oint_{S(\text{CE}_-(j, n))} \vec{h}_m^* \cdot \vec{ds} = 0, \quad m = 1, 2, 3, \quad (3.7)$$

and

$$\oint_{S(\text{CE}_+(j, n))} \vec{h}_m^* \cdot \vec{ds} = 0, \quad m = 1, 2, 3. \quad (3.8)$$

According to Figs. 3.2, 3.3a, and 3.3b, we have the following observations: (i) The edges  $\overline{CB}$  and  $\overline{CD}$  of  $\text{CE}_-(j, n)$  lie in  $\text{SE}(j - 1/2, n - 1/2)$ ; (ii) The edges  $\overline{AB}$  and  $\overline{AD}$  of  $\text{CE}_-(j, n)$  lie in  $\text{SE}(j, n)$ ; (iii) The edges  $\overline{ED}$  and  $\overline{EF}$  of  $\text{CE}_+(j, n)$  lie in  $\text{SE}(j + 1/2, n - 1/2)$ ; (iv) The edges  $\overline{AD}$  and  $\overline{AF}$  of  $\text{CE}_+(j, n)$  lie in  $\text{SE}(j, n)$ . As a result, with the aid of the numerical counterpart of Eq. (2.8), and Eqs. (3.1)–(3.6), we conclude that Eq. (3.7) leads to three relations (one for each  $m$ ) involving the independent unknowns  $\mathbf{U}_j^n$ ,  $(\mathbf{U}_x)_j^n$ ,  $\mathbf{U}_{j-1/2}^{n-1/2}$ ,  $(\mathbf{U}_x)_{j-1/2}^{n-1/2}$ , and Eq. (3.8) leads to another three relations, involving  $\mathbf{U}_j^n$ ,  $(\mathbf{U}_x)_j^n$ ,  $\mathbf{U}_{j+1/2}^{n-1/2}$ , and  $(\mathbf{U}_x)_{j+1/2}^{n-1/2}$ . Assuming that the unknowns at the mesh points  $(j - 1/2, n - 1/2)$  and  $(j + 1/2, n - 1/2)$  are given, the six components of  $\mathbf{U}_j^n$  and  $(\mathbf{U}_x)_j^n$  can be determined by the above six relations. It will be shown next how  $\mathbf{U}_j^n$  and  $(\mathbf{U}_x)_j^n$  can be determined from these relations without needing to solve any nonlinear algebraic equations.

Note that the space-time flux of  $\vec{h}^*$  leaving  $\text{CE}_-(j, n)$  through  $\overline{AD}$  and that leaving  $\text{CE}_+(j, n)$  through  $\overline{AD}$  are evaluated using the same unknowns, i.e.,  $\mathbf{U}_j^n$  and  $(\mathbf{U}_x)_j^n$ . Thus, these two space-time fluxes are each the negative of the other. As a result, a combination of Eq. (3.7) and Eq. (3.8) imply that

$$\oint_{S(\text{CE}(j, n))} \vec{h}_m^* \cdot \vec{ds} = 0, \quad m = 1, 2, 3, \quad (3.9)$$

where  $\text{CE}(j, n)$  (see Fig. 3.3(c)) is the union of  $\text{CE}_-(j, n)$  and  $\text{CE}_+(j, n)$ . Thus, the  $\text{CE}(j, n)$  are also conservation elements for the scheme. Here, as explained above, the fluxes of  $\vec{h}_m^*$  leaving  $\text{CE}(j, n)$  through  $\overline{CD}$ ,  $\overline{CB}$ ,  $\overline{ED}$ , and  $\overline{EF}$  can be evaluated in terms of  $\mathbf{U}_{j\pm 1/2}^{n-1/2}$  and  $(\mathbf{U}_x)_{j\pm 1/2}^{n-1/2}$ . Further, it can be shown that the flux of  $\vec{h}_m^*$  leaving  $\text{CE}(j, n)$  through  $\overline{BF}$  is simply  $(u_m)_j^n \Delta x$ . (This would not be true

on a nonuniform spatial mesh, but a small modification of the method, not described here, allows one to similarly avoid solving any nonlinear algebraic equations.) Thus, Eq. (3.9), which is a combination of Eqs. (3.7) and (3.8), implies that  $\mathbf{U}_j^n$  can be determined explicitly in terms of  $\mathbf{U}_{j\pm 1/2}^{n-1/2}$  and  $(\mathbf{U}_x)_{j\pm 1/2}^{n-1/2}$ . After obtaining  $\mathbf{U}_j^n$ ,  $\mathbf{F}_j^n$  and  $\mathbf{A}_j^n$  can be determined because they are functions of  $\mathbf{U}_j^n$  only. As a result, by applying either Eq. (3.7) or Eq. (3.8) (only one of these two equations is independent after Eq. (3.9) is used), one can obtain a system of three linear equations with the three unknowns being the three components of  $(\mathbf{U}_x)_j^n$ . In other words,  $(\mathbf{U}_x)_j^n$  can be determined in terms of  $\mathbf{U}_j^n$ ,  $\mathbf{U}_{j\pm 1/2}^{n-1/2}$ , and  $(\mathbf{U}_x)_{j\pm 1/2}^{n-1/2}$  by solving either Eq. (3.7) or Eq. (3.8).

### 3.3 Special Features of the CE/SE Method for Isentropic Flows

It has been shown by numerical experiments that the present scheme is neutrally stable in the interior of the computational domain up to at least a thousand time steps when the Courant number does not exceed unity. As a matter of fact, by using an analysis similar to that given at the end of Sec. 6 in [6], one can show that the linearized form of the present numerical analogue is neutrally stable when the Courant number does not exceed unity. Thus, the scheme described above is non-dissipative when the Courant number does not exceed unity. This has been shown in [2] to result from the fact that the numerical scheme shares with the Euler equations the property of being invariant under space-time inversion. The present scheme also meets the requirements of an ideal numerical analogue set forth in Sec. 2.3, i.e., it should be neutrally stable, explicit, and involving only two time levels.

From the previous development, it can be deduced that the numerical scheme observes a global conservation condition that is a direct result of Eq. (3.9), i.e., for any space-time region that is the union of any combination of the CEs of the type depicted in Fig. 3.3(c), the total flux of  $\vec{h}_m^*$ ,  $m = 1, 2, 3$ , leaving its boundary vanishes. Thus, the CE/SE scheme enforces global conservation of the numerical fluxes in both time and space.

The fluxes are uniquely defined at the boundaries of each CE. Each segment of the boundary of a CE lies in one and only one SE. This is made possible by the spatial staggering of the mesh points at one half-

time-level relative to those at the previous half-time-level. The conception of this staggered arrangement was in turn facilitated by the unified space-time viewpoint employed in the CE/SE method. This feature of unique definition of the interfacial fluxes allows us to avoid the need for upwind or other averaging of the fluxes at the interfaces. Thus the need for an exact or approximate Riemann solver does not arise. The flow of information between SEs is contained within the conservation law itself.

The CE/SE scheme does not require a flow gradient reconstruction strategy, for the simple reason that the flow gradients are themselves treated as unknowns, and are determined, together with the flow solution itself, from the discretized conservation equations, Eqs. (3.8) and (3.9). No unnecessary assumption of smoothness of the solution between SEs is made in the Euler isentropic-flow scheme, when calculating either the flow variables or the flow gradients. While conventional finite-volume techniques also allow for the flow variables to be discontinuous, by using conservation to link cells, they do assume continuity of the flow when reconstructing the gradient and when using upwind biasing to calculate the interfacial fluxes. Contrarily, in the CE/SE scheme, no such assumptions are required, and consequently no complex flux-limiter strategy is needed. In some finite-element schemes, even more constraining assumptions of solution smoothness are made; the solution itself is taken to be continuous between cells by choosing to place single-valued solution nodes on the interfaces of cells.

### 3.4 The Shock-Capturing Scheme

The above marching scheme for isentropic flows can be expressed as

$$\begin{aligned} \mathbf{U}_j^n = \\ \mathbf{H} \left( \mathbf{U}_{j-1/2}^{n-1/2}, \mathbf{U}_{j+1/2}^{n-1/2}, (\mathbf{U}_x)_{j-1/2}^{n-1/2}, (\mathbf{U}_x)_{j+1/2}^{n-1/2} \right), \quad (3.10) \end{aligned}$$

and

$$\begin{aligned} (\mathbf{U}_x)_j^n = \\ \mathbf{H}_x \left( \mathbf{U}_{j-1/2}^{n-1/2}, \mathbf{U}_{j+1/2}^{n-1/2}, (\mathbf{U}_x)_{j-1/2}^{n-1/2}, (\mathbf{U}_x)_{j+1/2}^{n-1/2} \right) \quad (3.11) \end{aligned}$$

Here  $\mathbf{H}$  and  $\mathbf{H}_x$  are column-matrix functions. Their explicit forms can be obtained from Eqs. (5.20)-(5.29) in [6] with the assumption that the viscosity  $\mu = 0$ . In the construction of the shock-capturing scheme, the local conservation condition, Eq. (3.9), is again assumed. Because Eq. (3.10) follows directly

from Eq. (3.9), the former is incorporated into the shock-capturing scheme without modification. As a result, given the same  $\mathbf{U}_{j\pm 1/2}^{n-1/2}$  and  $(\mathbf{U}_x)_{j\pm 1/2}^{n-1/2}$ , the shock-capturing scheme shares with the non-dissipative scheme the same zero-order terms on the right sides of Eqs. (3.1) and (3.2). In addition, the shock-capturing scheme also observes a global conservation condition that is also a direct result of Eq. (3.9).

The shock-capturing scheme is obtained by modifying Eq. (3.11). To proceed, let

$$(\mathbf{U}')_{j\pm 1/2}^n = \mathbf{U}_{j\pm 1/2}^{n-1/2} + \frac{\Delta t}{2} (\mathbf{U}_t)_{j\pm 1/2}^{n-1/2}, \quad (3.12)$$

i.e.,  $(\mathbf{U}')_{j\pm 1/2}^n$  is a first-order Taylor's approximation of  $\mathbf{U}$  at the point  $(j \pm 1/2, n)$ . Thus,

$$(\mathbf{U}_x)_j^n = \frac{(\mathbf{U}')_{j+1/2}^n - (\mathbf{U}')_{j-1/2}^n}{\Delta x} \quad (3.13)$$

is a central-difference approximation of  $\mathbf{U}_x$  at the mesh point  $(j, n)$ . In the shock-capturing scheme, Eq. (3.11) is replaced by

$$(\mathbf{U}_x)_j^n = (1 - 2\epsilon)(\mathbf{H}_x)_j^n + 2\epsilon(\mathbf{U}_x^c)_j^n, \quad (3.14)$$

where  $(\mathbf{H}_x)_j^n$  denotes the expression on the right side of Eq. (3.11), and  $\epsilon$  is a real number. Note that  $(\mathbf{U}_x^c)_j^n$  is defined in terms of a central-difference approximation. Generally, numerical dissipation is introduced as a result of using such an approximation. On the other hand,  $(\mathbf{H}_x)_j^n$  represents the solution from a non-dissipative scheme. The right side of Eq. (3.14) is a weighted averaged of  $(\mathbf{H}_x)_j^n$  and  $(\mathbf{U}_x^c)_j^n$  with the weight factor of  $1 - 2\epsilon$  and  $2\epsilon$ , respectively. Therefore, one may heuristically conclude that the numerical dissipation associated with the shock-capturing scheme can be increased by increasing the value of  $\epsilon$ . This conclusion is verified by numerical experiments. As shown in [6], the stability domain of the shock-capturing scheme is defined by

$$CFL \leq 1 \quad \text{and} \quad 0 \leq \epsilon \leq 1, \quad (3.15)$$

where  $CFL$  is the maximum Courant number. Note that Eq. (3.14) can also be expressed as

$$(\mathbf{U}_x)_j^n = (\mathbf{H}_x)_j^n + 2\epsilon(D\mathbf{U})_j^n, \quad (3.16)$$

or

$$(\mathbf{U}_x)_j^n = (\mathbf{U}_x^c)_j^n + (2\epsilon - 1)(D\mathbf{U})_j^n, \quad (3.17)$$

where

$$(D\mathbf{U})_j^n \equiv (\mathbf{U}_x^c)_j^n - (\mathbf{H}_x)_j^n. \quad (3.18)$$

According to Eq. (3.16),  $(\mathbf{U}_x)_j^n$  for the shock-capturing scheme is the sum of the non-dissipative term  $(\mathbf{H}_x)_j^n$  and the dissipative term  $2\epsilon(D\mathbf{U})_j^n$ . The latter provides the necessary entropy-increasing condition within the stability domain defined by Eq. (3.15). Also it is seen from Eqs. (3.16) and (3.17) that  $(\mathbf{U}_x)_j^n$  reduces to  $(\mathbf{H}_x)_j^n$  and  $(\mathbf{U}_x^c)_j^n$  in the cases of  $\epsilon = 0$  and  $\epsilon = 0.5$ , respectively.

The shock-capturing scheme described above generally can capture shocks with high resolution and without generating substantial numerical oscillations near shock if  $0.3 \leq \epsilon \leq 0.8$ . To further damp out these oscillations,  $(\mathbf{U}_x^c)_j^n$  in Eq. (3.17) (which is equivalent to Eq. (3.14)) can be modified using a simple slope-limiting procedure [6]. Let

$$(\mathbf{U}_{x\pm})_j^n = \pm \frac{(\mathbf{U}')_{j\pm 1/2}^n - \mathbf{U}_j^n}{\Delta x/2}. \quad (3.19)$$

Because  $(\mathbf{U}')_{j\pm 1/2}^n$  and  $\mathbf{U}_j^n$  are the numerical analogues of  $\mathbf{U}$  at the mesh points  $(j \pm 1/2, n)$  and  $(j, n)$ , respectively,  $(\mathbf{U}_{x+})_j^n$  and  $(\mathbf{U}_{x-})_j^n$  are two numerical analogues of  $\mathbf{U}_x$  at the mesh point  $(j, n)$ , with one being evaluated from the right and another from the left. It follows from Eqs. (3.13) and (3.19) that

$$(\mathbf{U}_x^c)_j^n = \frac{1}{2} [(\mathbf{U}_{x+})_j^n + (\mathbf{U}_{x-})_j^n], \quad (3.20)$$

i.e.,  $(\mathbf{U}_x^c)_j^n$  is the simple average of  $(\mathbf{U}_{x+})_j^n$  and  $(\mathbf{U}_{x-})_j^n$ . A nonlinear weighting function is defined as

$$W(x_-, x_+; \alpha) = \frac{|x_+|^\alpha x_- + |x_-|^\alpha x_+}{|x_+|^\alpha + |x_-|^\alpha} \quad (3.21)$$

where  $x_-$ ,  $x_+$ , and  $\alpha$  are real variables with  $|x_+| + |x_-| > 0$  and  $\alpha \geq 0$ . Note that (i)  $W(x_-, x_+; 0)$  is the simple average of  $x_-$  and  $x_+$ , and (ii)  $W(x_-, x_+; 1)$  and  $W(x_-, x_+; 2)$  are used in the slope-limiters proposed by van Leer [40] and van Albeda et al. [50], respectively.

Recall that  $(u_{mx\pm})_j^n$  denotes the  $m$ -th component of  $(\mathbf{U}_{x\pm})_j^n$ . Let

$$(u_{mx}^w)_j^n = W [(u_{mx-})_j^n, (u_{mx+})_j^n, \alpha] \quad (3.22)$$

Then, as shown in [6], numerical oscillations near shocks can be suppressed very efficiently if  $(\mathbf{U}_x^c)_j^n$  in Eq. (3.17) is replaced by  $(\mathbf{U}_x^w)_j^n$ , i.e., the column matrix formed by  $(u_{mx}^w)_j^n$ ,  $m = 1, 2, 3$ , if  $\alpha \geq 1$ .

### 3.5 Concluding Remarks

We conclude this section on the CE/SE method in 1D by mentioning that 1D CE/SE explicit solvers

have been developed for the scalar advection equation (with and without controllable added numerical dissipation), and for the scalar advection-diffusion equation. Corresponding schemes have been formulated for the Euler and Navier-Stokes equations. The Euler schemes were described in this section. Implicit schemes have also been formulated for the 1D advection-diffusion equation. The various schemes for the scalar equations have been thoroughly analysed for their accuracy and stability properties, see [6] and [8]. Surprisingly, various limiting cases of the 1D scalar schemes turn out to have amplification factors matching those of several classical numerical schemes, viz., the Leapfrog, Lax, DuFort-Frankel and Crank-Nicolson schemes.

The numerical boundary conditions have not been discussed in this paper. The boundary conditions used to date have been both simple and effective. The flux-based nature of the method allows, in particular, the use of extremely simple yet robust non-reflecting boundary conditions [12]. The efficacy of these non-reflecting boundary conditions is demonstrated in some of the numerical examples in this paper. Further research is under way on boundary conditions for the CE/SE schemes.

## 4 The 2D Euler Solvers

In Sec. 3, it was established that in the 1D case there were only *two* sets of independent marching variables, i.e., (i)  $(u_m)_j^n$ ,  $m = 1, 2, 3$ , and (ii)  $(u_{mx})_j^n$ ,  $m = 1, 2, 3$ , at each mesh point  $(j, n)$ , if Eqs. (3.1)–(3.6) are assumed. As a result, it requires *two* sets of conservation conditions, i.e., Eqs. (3.7) and (3.8) to construct the 1D non-dissipative Euler scheme. As a prerequisite to Eqs. (3.7) and (3.8), *two* CEs, i.e.,  $\text{CE}_-(j, n)$  and  $\text{CE}_+(j, n)$  are defined for each mesh point  $(j, n)$ .

The 2D CE/SE non-dissipative Euler solver [5, 7] was constructed using the same set of design principles that was used to construct its 1D counterpart. The differences between them stem entirely from the fact that there is one more spatial dimension to be considered in the 2D solver. In this section, only the basic geometric structures of the 2D solver will be described. For other details, the reader is referred to [5].

The 2D unsteady Euler equations of a perfect gas [5, 7] consist of *four* independent equations,  $m = 1,$

2, 3, 4, instead of the *three* equations applicable to 1D flow. Also, in the 2D case, there are two spatial components of the gradient of each  $u_m$  (i.e.,  $u_{mx}$  and  $u_{my}$ , where  $x$  and  $y$  are Cartesian coordinates for the 2D space). This is in contrast to the 1D case, in which, for each  $u_m$ , there is only one spatial component of the gradient of  $u_m$  (i.e.,  $u_{mx}$ ).

In the development of the 2D non-dissipative Euler solver and its extensions [5], a set of equations that is a natural 2D extension of Eqs. (3.1)–(3.6) is assumed. As a result, there are *three* sets of independent marching variables at each mesh point  $(j, k, n)$  (see Figs. 4.1 and 4.2 for the locations of the mesh points. The reader is referred to [5, 7] for the definitions of the spatial mesh indices  $j$  and  $k$  of the uniform structured triangular mesh of Fig. 4.1). They are  $(u_m)_{j,k}^n$ ,  $(u_{mx})_{j,k}^n$  and  $(u_{my})_{j,k}^n$ ,  $m = 1, 2, 3, 4$ . It follows that it requires *three* sets of conservation conditions (each set comprises four conditions, corresponding to  $m = 1, 2, 3, 4$ ) at each mesh point to construct the 2D non-dissipative solver. Therefore, as a prerequisite, one must define *three* conservation elements for each mesh point. The construction of these CEs, which is the most intriguing part of the development of the 2D CE/SE Euler solver, will be described in what immediately follows.

Consider a spatial domain formed by congruent triangles (see Fig. 4.1). The center of each triangle is marked by either an empty circle or a filled circle. The distribution of these empty and filled circles is such that if the center of a triangle is marked by a filled (empty) circle, then the centers of the three neighboring triangles with which the first triangle shares a side are marked by empty (filled) circles. As an example, point  $G$ , the center of the triangle  $\Delta BDF$ , is marked by a filled circle while points  $A$ ,  $C$  and  $E$ , the centers of the triangles  $\Delta BFM$ ,  $\Delta BJD$  and  $\Delta DLF$ , respectively, are marked by empty circles. These centers are the spatial projections of the space-time mesh points used in the 2D solver [5, 7].

To specify the exact locations of the mesh points in space-time, one must also specify their temporal coordinates. In the 2D CE/SE development, again we assume that the mesh points are located at the time levels  $n = 0, \pm 1/2, \pm 1, \pm 3/2, \dots$ , with  $t = n \Delta t$  at the  $n$ th time level. Furthermore, we assume that the spatial projections of the mesh points at a whole-integer (half-integer) time level are the points marked by empty (filled) circles in Fig. 4.1.

Let the triangles depicted in Fig. 4.1 lie on the time level  $n = 0$ . Then those points marked by

empty circles are the mesh points at this time level. On the other hand, those points marked by filled circles are not the mesh points at the time level  $n = 0$ . They are only the spatial projections of the mesh points at half-integer time levels. Thus the 2D space-time mesh is, as in the 1D case, a staggered mesh.

Points  $A$ ,  $C$  and  $E$ , which are depicted in Figs. 4.1 and 4.2, are three mesh points at the time level  $n = 0$ . Point  $G'$ , which is depicted in Fig. 4.2, is a mesh point at the time level  $n = 1/2$ . Its spatial projection at the time level  $n = 0$  is point  $G$ . Because point  $G$  is not a mesh point, it is not marked by a filled circle in the space-time plot given in Fig. 4.2. Hereafter, only a mesh point, e.g., point  $G'$ , will be marked by a filled or empty circle in a space-time plot.

The conservation elements associated with point  $G'$  are defined to be the space-time quadrilateral cylinders  $GFABG'F'A'B'$ ,  $GBCDG'B'C'D'$ , and  $GDEFG'D'E'F'$  that are depicted in Fig. 4.2. Here (i) points  $B$ ,  $D$  and  $F$  are the vertices of the triangle with point  $G$  being its center (centroid) (see also Fig. 4.1), and (ii) points  $A'$ ,  $B'$ ,  $C'$ ,  $D'$ ,  $E'$  and  $F'$  are on the time level  $n = 1/2$  with their spatial projections on the time level  $n = 0$  being points  $A$ ,  $B$ ,  $C$ ,  $D$ ,  $E$  and  $F$ , respectively.

Recall that, in the development of the 1D non-dissipative Euler solver, a pair of diagonally opposite vertices of each  $CE_{\pm}(j, n)$  (see Figs. 3.3(a) and (b)) are assigned as mesh points. Furthermore, the boundary of each  $CE_{\pm}(j, n)$  is a subset of the union of the SEs associated with the two diagonally opposite mesh points of this CE. In the 2D development, as seen from Figs. 4.2, two diagonally opposite vertices of each CE are also assigned as mesh points. In the following, we shall define the SEs such that even in the 2D case, the boundary of a CE is again a subset of the union of the SEs associated with the two diagonally opposite mesh points of this CE.

As an example, the SE associated with point  $G'$  is depicted in Fig. 4.3. It is the union of three vertical rectangles (i.e.,  $G''B''BG$ ,  $G''D''DG$  and  $G''F''FG$ ), a horizontal hexagon (i.e.,  $A'B'C'D'E'F'$ ) and their immediate neighborhood. Note that points  $G''$ ,  $B''$ ,  $D''$  and  $F''$  are on the time level  $n = 1$  and their spatial projections on the time level  $n = 0$  are points  $G$ ,  $B$ ,  $D$  and  $F$ , respectively. The definition of the SE of any mesh point is similar to the definition of the SE of the point  $G'$ . Note that on the uniform structured mesh shown, the SEs and CEs at the whole integer time levels can be seen to be congruent to the SEs and CEs respectively at the

half integer time levels, by a rotation of 180 degrees about the time axis followed by spatial and temporal translations.

As depicted in Fig. 4.2, one of the CEs associated with point  $G'$  is the space-time quadrilateral cylinder  $GFABG'F'A'B'$ . Among the vertices of this CE, only points  $A$  and  $G'$  are mesh points. From Figs. 4.3, it is seen that (i) three of the faces of this CE, i.e.,  $GBG'B'$ ,  $GG'F'F$  and  $G'F'A'B'$  are subsets of the SE of point  $G'$ , and (ii) the other three faces, i.e.,  $AA'F'F$ ,  $ABB'A'$  and  $ABGF$  are subsets of the SE of point  $A$ . As a result, by assuming that the flux of each  $\bar{h}_m^*$  ( $m = 1, 2, 3, 4$ ) is conserved over this CE, one can impose four conditions involving only the independent marching variables at the mesh points  $A$  and  $G'$ . Similarly, by using the flux conservation conditions over the other two CEs associated with point  $G'$ , one can obtain eight other conditions that relate the independent marching variables at the mesh points  $G'$ ,  $C$  and  $E$ . Using the above 12 conditions, the 12 independent marching variables, i.e.,  $u_m$ ,  $u_{mx}$  and  $u_{my}$ ,  $m = 1, 2, 3, 4$ , at the mesh point  $G'$  can be determined in terms of the independent marching variables at the mesh points  $A$ ,  $C$  and  $E$ . By considering the mesh point  $G'$  as a typical mesh point, the reader can understand how the 2D non-dissipative Euler solver was constructed [5, 7].

The non-dissipative Euler solver is only one of several 2D solvers described in [5, 7]. The latter document includes the 2D extensions of all but one of the 1D solvers described in [6]. The only exception is the 2D extension of the 1D Navier-Stokes solver. This is under development, and will be dealt with in a separate paper. Also, because of the similarity in their design, each of the 2D extensions shares with its 1D version virtually the same fundamental characteristics. As an example, the 2D non-dissipative Euler solver is neutrally stable, explicit, and involves only two time levels during a single time step. It also preserves the forward-backward marching nature and the space-time inversion invariance property of the 2D unsteady Euler equations. These are the same properties that characterize the 1D non-dissipative Euler solver.

The discussion of the 2D Euler solvers is concluded with the following remarks:

1. Because (i) the spatial geometric structure embedded in the CE/SE 2D space-time mesh is constructed from triangles, and (ii) triangles

are the simplest polygon in the 2D space, the CE/SE solvers described in [5] can easily be modified and extended to solve flow problems with complex geometries using unstructured triangular spatial meshes[31].

2. Several 2D CE/SE solvers using nonuniform mesh have been developed [22–29]. Some of the numerical results generated with these solvers will be presented in Sec. 6.
3. The extension of the non-dissipative Euler solver to become a shock-capturing scheme by the addition of controllable numerical dissipation is a straightforward extension of the development in Eqs. (3.10) – (3.22).
4. The non-reflecting boundary conditions mentioned in the previous section have also easily been extended (e.g., [13, 30]) to the 2D case, and have proven to be just as effective as in 1D

## 5 The Basis for a 3D Euler Solver

We indicate the discretization of space-time which forms the basis for a 3D Euler solver currently under development. The extension of the CE/SE method to three spatial dimensions follows reasoning similar to that used when extending the 1D solver to the 2D case (see the previous section). In the 3D case, the unsteady Euler equations of a perfect gas consist of five independent equations,  $m = 1, 2, 3, 4, 5$ . There are *three* spatial components of the gradient of each  $u_m$  (i.e.,  $u_{mx}$ ,  $u_{my}$  and  $u_{mz}$ , where  $x$ ,  $y$  and  $z$  are Cartesian coordinates for the 3D space). When piecewise linear variation with space and time are assumed for the numerical solution, as is done in the 1D and 2D cases, and after the differential equation is assumed valid at each mesh point, there remain *four* sets of independent marching variables at each mesh point. It follows that *four* sets of conservation conditions are required at each mesh point to construct the non-dissipative 3D solver. Hence, *four* conservation elements must be defined for each mesh point. Just as a triangle was the polygon sharing its bounding edges with three neighbors, so a tetrahedron is the polyhedron sharing its bounding surfaces with *four* neighbors.

In the 2D case, referring to Figs. 4.1 and 4.2,  $GFAB$ ,  $GBCD$  and  $GDEF$  are the spatial projections of the CEs associated with  $G'$ . The CEs in

the 3D case can be constructed in analogous fashion. Consider the tetrahedron  $ABCD$  with centroid  $G$ , and the tetrahedron  $ABCP$  with centroid  $H$ , depicted in Fig. 5.1. They share the face  $ABC$ . The polyhedron  $GABCH$  is then defined as the spatial projection of a CE associated with a point  $G'$ . The CE is thus a right cylinder in space-time, with  $GABCH$  as its spatial base. The point  $G$  is the spatial image of the mesh point  $G'$ , which is displaced temporally from  $G$  by half a time step.

In similar fashion, three additional CEs associated with the mesh point  $G'$  can be constructed by considering in turn three tetrahedra that share with  $ABCD$  one of its other three faces. Thus the numerical solution at  $G'$  can be determined from a knowledge of the solution at the four mesh points (one of which is  $H$ ) which are the centroids of the tetrahedra sharing a face with  $ABCD$ . This forms the basis of a non-dissipative 3D Euler solver.

Just as the structured mesh of Fig. 4.1 is obtainable by sectioning the parallelograms of Fig. 4.1 into triangles, so it is possible to construct a structured mesh of tetrahedra by sectioning a mesh of parallelepipeds. Details of the construction will be given in a future paper. Again, the extension to a space-time mesh built from an unstructured tetrahedral spatial mesh is simple.

## 6 Computational Examples

### 6.1 Shock Tube with Non-Reflecting Computational Boundaries

The CE/SE computational results are presented for an extended Sod's shock tube problem [51], in which the shock tube problem is extended by imposing a non-reflecting boundary condition at each end of the computational domain. The challenge of the non-reflective boundary condition is no less difficult than that of capturing the shock and the contact discontinuity. First, the flow under consideration is subsonic throughout and the treatment of the non-reflecting boundary condition for a subsonic flow is more difficult than that for a supersonic flow. Second, this difficulty is exacerbated by the existence of a shock and a contact discontinuity, which must be allowed to exit the domain without reflection.

Flow of an ideal gas with specific-heat ratio  $\gamma =$

1.4 is considered in an infinite shock-tube. The initial condition, at time  $t = 0$ , is  $(\rho, v, p) = (1, 0, 1)$  if  $x < 0$ , and  $(\rho, v, p) = (0.125, 0, 0.1)$  if  $x > 0$ . Here,  $\rho, v, p$  denote the density, velocity, and pressure of the fluid, respectively. A uniform space-time mesh with  $\Delta x = 0.01$  and  $\Delta t = 0.004$  (corresponding to a maximum Courant number of about 0.88) is used over the computational domain defined by  $-0.5 \leq x \leq 0.5$  and  $t \geq 0$ . The settings  $\epsilon = 0.5$  and  $\alpha = 1$  are used for the artificial dissipation parameters. Note that the results are obtained without the need of any local mesh-refinement techniques or any time-step tuning.

The non-reflecting boundary conditions used are (i)  $\mathbf{U}_j^n = \mathbf{U}_{j-1/2}^{n-1/2}$  and  $(\mathbf{U}_x)_j^n = (\mathbf{U}_x)_{j-1/2}^{n-1/2}$  if  $(j, n)$  is a mesh point on the right boundary, and (ii)  $\mathbf{U}_j^n = \mathbf{U}_{j+1/2}^{n-1/2}$  and  $(\mathbf{U}_x)_j^n = (\mathbf{U}_x)_{j+1/2}^{n-1/2}$  if  $(j, n)$  is a mesh point on the left boundary. The reasons why such trivial extrapolations can serve so well as non-reflecting boundary conditions in the CE/SE method are explained in a separate paper [12].

Figs. 6.1–6.3 show the numerical solution (triangular data points) compared with the analytical solution (unbroken line) at three different times, namely,  $t = 0.2, 0.4$  and  $0.6$ . It is seen that excellent agreement is obtained between the numerical results and the analytical solution. In particular, as seen in Fig. 6.1, the shock wave discontinuity is resolved almost within one mesh interval and the contact discontinuity is resolved in four mesh intervals. Fig. 6.2 shows that by  $t = 0.4$ , the numerically computed shock wave has passed cleanly through the right boundary, with no spurious reflections. Similarly, Fig. 6.3 shows that by  $t = 0.6$ , the contact discontinuity has passed through the right boundary, while the expansion region has partially passed through the left boundary. Agreement with the exact solution continues to be excellent.

### 6.2 Convection-Diffusion Examples

The CE/SE computations described in this subsection were originally presented in [8], where an implicit CE/SE solver for the convection-diffusion equation  $u_t + au_x - \mu u_{xx} = 0$  ( $\mu \geq 0$ ) was developed. The solver, termed the  $a$ - $\mu$ (I1) solver, is an extension of the  $a$  scheme, which is the CE/SE solver for  $u_t + au_x = 0$ . The examples below help show that the scheme is accurate over the whole Reynolds number range, from pure diffusion to convection-

dominated solutions.

**Pure Diffusion.** We consider a special case of the convection-diffusion equation with  $a = 0$  and  $\mu = 1$ , in the domain  $0 \leq x \leq 1$  and  $t \geq 0$ . The initial/boundary conditions completing the problem specification are (i)  $u(0, t) = u(1, t) = 0$  for  $t \geq 0$ , (ii)  $u(x, 0) = 2x$  for  $0 \leq x \leq 0.5$ , and (iii)  $u(x, 0) = 2(1 - x)$  for  $0.5 \leq x \leq 1$ . The solution  $u(x, t)$  exhibits the diffusive decay of the initial sawtooth shape. An exact series solution is available, see for e.g. p.15 of [52]. For the CE/SE computation, uniform mesh intervals  $\Delta x = 0.02$  and  $\Delta t = 0.005$  are used. Fig. 6.4 shows the time-slice at  $t = 0.05$ , comparing numerical and exact solutions, and also showing the error scaled with the peak exact value at that time level. The maximum error magnitude is seen to be about 0.5% of the peak solution value. At  $t = 1$  (not shown), when the peak solution value has dwindled to about  $4 \times 10^{-5}$ , the maximum error magnitude is about 0.15% of the peak solution value.

**Boundary Layer,  $Re = 100$ .** We next consider the problem defined for the convection-diffusion equation in the domain  $0 \leq x \leq 1$  and  $t \geq 0$  by the conditions (i)  $u(0, t) = 0$  for  $t \geq 0$ , (ii)  $u(1, t) = 1$  for  $t \geq 0$ , and (iii)  $u(x, 0) = x$  for  $0 \leq x \leq 1$ . The ‘steady-state’ or time-asymptotic limit of the solution is  $u(x, \infty) = [\exp(ax/\mu) - 1] / [\exp(a/\mu) - 1]$ . The case  $a = 1$ ,  $\mu = 0.01$  (i.e.  $Re = 100$ ) is considered, which leads to a steady-state boundary layer at  $x = 1$ . Uniform mesh intervals  $\Delta x = 0.0025$  and  $\Delta t = 0.002$  are used, so that the Courant number is 0.8. Fig. 6.5 shows the computed and exact steady-state limits, together with the error. The boundary layer is seen to be well resolved, with the maximum magnitude of the error being about 1% of the solution peak.

### 6.3 Unstable ZND Detonation Wave

#### 1 The Piston Problems

We consider 1D and 2D ZND detonation wave problems. The governing equations consist of the Euler equations together with an equation for the reactant concentration, with a stiff source term in it. For details of the treatment of source terms in the present CE/SE method, we refer the reader to [18].

The initial condition of the present calculation is

a long tube filled with reactant with a piston on one end moving at a constant speed into the quiescent reactant. Here, we use the piston face as the origin of the coordinate system. In this coordinate frame, reactant is charged into a closed-end tube at a constant speed. A shock wave is reflected on the closed end to ignite the reactant.

The parameters of the flow field in the present calculation are set as chemical potential  $q_0 = 50$ , activation energy  $E^+ = 50$ , specific heat ratio  $\gamma = 1.2$ , and the over drive coefficient  $f = 1.6$ . According to the classical theory for detonation instability, the detonation wave becomes unstable and a longitudinal wave bouncing between the piston and the shock front should be observed. In this calculation, only 5 mesh nodes are used in the each half-reaction zone. In Fig. 6.6(a), we show the temporal evolution of the pressure level at the shock front. The first pressure jump in the figure is caused by the start-up process of the pushing piston. After the first pressure jump, the flow field settles down and the instability waves gradually built up. After 40 time units, a remarkable instability wave occurs. In about 60 time unit, there are about 8 pressure peaks. This numerical solution is in excellent agreement with the results reported by Fickett and Wood [53].

#### 2 Numerical structure for two-dimensional detonations

Unstable detonation waves obtained with the 2D Euler equations plus a ZND equation are computed by S.T. Yu and S.J. Park, in work yet to be published. Fig. 6.6(b) is a Schlieren-type image of detonation waves, especially plotted two periods for pressure. A detonation is traveling from the top to the bottom and the flowfield is composed of: (i) the quiescent state of the reactant before the shock, (ii) a von Neumann spike with finite rate reaction, and (iii) the equilibrium state after the reaction zone. The two-dimensional cellular structure of detonation waves is of concern: that is, the wave patterns that arise when the flow parameters are chosen such that the flow field is unstable. The parameters of the flow field in the present calculation are set as  $q_0 = 50$ ,  $E^+ = 50$ ,  $\gamma = 1.2$ , and the over drive coefficient  $f = 1.6$ . According to the classical theory for detonation instability, an unstable detonation wave should be obtained with these parameters.

In this calculation, 20 mesh nodes are used in the half reaction zone (260 mesh cells covered the width of the channel). The calculation of two-dimensional detonation wave is initiated by placing a

one-dimensional solution on a two-dimensional mesh with periodic boundary conditions along the left and right of the flow. Without artificial perturbation, the shock front quickly becomes unstable under flow conditions receptive for instability. Crisp cellular structure is observed after transverse waves cause the shock front to be curved. This figure shows that regular mach stem cell structure exists between two curved strong incident shocks and that peak pressure zone is around triple points in the cellular structure for unstable detonations.

The results compared favorably with the previously reported data. These results show that the CE/SE method is a very accurate method for direct calculations of propagating detonation waves. Figure 6.6(b) is obtained at  $t = 12.5\text{sec}$ .

#### 6.4 Diffraction of a Shock Wave around a Wedge

According to the experimental shadowgraph results shown in [54], when a plane shock wave of  $M_s = 1.3$  is moving over the beginning of a finite wedge of semi-vertex angle  $\theta = 26.565^\circ$ , an ordinary Mach reflection is generated. As the shock wave passes the base, the flow separates to form vortex sheets at the sharp corners. Further interaction produces an increasingly elaborate pattern of shock waves, slip lines and vortices.

As reported in [22, 26], this flowfield is simulated using the CE/SE Euler solver. By virtue of the symmetry in the solution, attention is restricted to the upper half of the domain. The extent of the computational domain is set based on an estimation from Fig. 522 in [54]. The shock wave is at  $x = -0.5$  at  $t = 0$ . The numerical boundary condition imposed on the vertical wall of the wedge is described in [25]. Numerical solutions at eight time levels ( $t = 0.725, 0.9075, 1.2125, 1.55, 1.825, 2.1375, 2.4875$ ; and  $2.9475$ ), obtained by using two subdomains with  $321 \times 89$  and  $209 \times 34$  mesh points, and with  $\Delta t = 0.0025$ , are shown in Fig. 6.7. It should be pointed out that the upper and lower walls of the channel shown in the shadowgraphs of [54] are actually further apart than the top and bottom edges of the shadowgraphs. Therefore some flow phenomena that are seen in Fig. 6.7, in the region near the upper wall, are lost in shadowgraphs, especially at the 4th time level. Comparisons of the computed solutions with experimental pictures of [54] have shown an excellent agreement in general flow features except for

those phenomena induced by the effect of viscosity. The shock waves, slip lines and vortices are captured very well.

#### 6.5 Implosion/Explosion of Polygo-nal Shock Waves in a Box

The 2-D CE/SE Euler solver has been used in [27] to solve a problem studied in [55], concerning the implosion/explosion of a polygonal shock wave in a square box. In addition to the early stage of the implosion/explosion process, the later development of the process, which was not studied in [55], is also simulated in [27]. The computation further demonstrates the robustness of the CE/SE Euler scheme in handling discontinuous flows.

A uniformly distributed  $241 \times 241$  grid is utilized in the computational domain, which is a square defined by  $-2 \leq x \leq 2$  and  $-2 \leq y \leq 2$ . The initial shock wave configuration is a polygon, the geometric center of which coincides with that of the square. Inside the polygon is a low pressure region, with a pressure ratio of 10 across the shock. The radius of the circumscribed circle of the polygon is selected to be  $0.8\sqrt{3}$  for all shapes of the polygon. In the numerical scheme, the two parameters  $\epsilon$  and  $\alpha$  are set to be 0.5 and 1 respectively, everywhere in the computational domain for all cases, and the maximum Courant number is always kept at a value of 0.9.

In one set of computations, the early flowfield is studied for polygonal shock waves with initial shapes of an equilateral triangle, a square, and a pentagon. The density contour plots at different time levels are shown in Fig. 6.8. Wave patterns similar to those captured in Figs. 1–5 of [55] using a TVD method on a  $359 \times 359$  grid are clearly shown in the CE/SE solutions, displaying detailed features such as Mach stems and the newly-developed smaller polygons.

In another computation, the implosion/explosion of a hexagonal shock wave is simulated until the re-implosion of the shock wave is observed in the box. More complex flow phenomena can be seen in the density contour plots of Fig. 6.9, including the reflections of shock waves, shock-shock interaction, and shock-contact surface interaction. It is interesting to note that the shape of the contact surface centered at the origin of the box remains unchanged even after the passage of shock waves.

## 6.6 Examples from Computational Aeroacoustics

The CE/SE computational examples we describe in the next two subsections were reported in [16] and [15]. The investigations in [16] and [15] found the CE/SE Euler scheme to be capable of handling the complete spectrum of flows, from small-amplitude linear acoustic waves, all the way to nonlinear or even discontinuous waves (shocks). Through numerical experiments in computational aeroacoustics, the following salient properties of the CE/SE Euler scheme emerge: (i) The CE/SE scheme possesses very low dispersion error and yields high resolution results comparable to that of a high order compact difference scheme, although nominally the CE/SE scheme is only of 2nd order accuracy. (ii) In general, the numerical non-reflecting boundary condition applicable to the CE/SE scheme is genuinely multi-dimensional, and can be implemented in a simple and elegant way without resorting to the complexities of characteristic forms or buffer zones. (iii) The CE/SE scheme is both a CFD (Computational Fluid Dynamics) and a CAA (Computational Aeroacoustics) scheme, capable of handling continuous and discontinuous flows. It thus represents a unique numerical technique for flows where sound waves and shocks and their interactions are important.

It is well-known that in CAA, the non-reflecting boundary condition plays a dominant role in the final numerical results. In general, there are three ways to impose the non-reflecting boundary conditions, namely,

- (i) to apply 1-D characteristic variables (Riemann invariants) in the direction normal to the boundary,
- (ii) to minimize spurious numerical reflections from the boundaries by inserting a buffer zone with increased numerical damping,
- (iii) to apply an asymptotic analytical solution at the boundaries.

In the new CE/SE scheme, none of the above complex treatments of non-reflecting boundary conditions is needed. Instead, one of several possible simple non-reflecting boundary conditions is:

$$(u_{mx})_{j,k}^n = (u_{my})_{j,k}^n = 0, \quad m = 1, 2, 3, 4,$$

while  $(u_m)_{j,k}^n$  is defined by zeroth order extrapolation from the interior neighbors. In general, the

consequent reflection amounts to about 1% of the strength of the incident waves.

## 6.7 Multiple interaction of strong vortex and shocks

In the first example, the multiple interaction of a strong vortex and shocks is considered. It is demonstrated as a typical example to show that the CE/SE scheme is capable of handling not only the linear waves but also the highly nonlinear waves as well. It is well-known that interaction between a vortex and a shock may generate acoustic waves. To our knowledge, researches including both experimental and numerical computation, are mostly concentrated in a single interaction between a vortex and a normal shock. In this problem, we intend to show the capability of the CE/SE method in handling complicated wave interactions. Although there are no existing experimental results for comparison, our numerical result appears consistent with the physical phenomena. A grid of  $401 \times 101$  is employed in this problem with  $\Delta x = \Delta y = 1$ . The inflow boundary condition is given as a supersonic flow of Mach 2.9:

$$u_0 = 2.9, \quad v_0 = 0, \quad p_0 = 1/1.4, \quad \rho_0 = 1$$

boundary condition at the top is an inclined flow:

$$u_t = 2.6193, v_t = -0.50632, p_t = 1.5282, \rho_t = 1.7000$$

The outflow boundary condition is of the non-reflecting variety and the bottom boundary is a solid reflecting wall. Then, a steady oblique shock is formed with  $29^\circ$  inclination and reflected at the bottom wall. The flow with shocks is precalculated until a steady state is reached. It is then used as the background mean flow for further computation. At  $t = 0$ , a strong Lamb's vortex is placed at  $x = 22$ ,  $y = 60$ . The following is a brief description for a stationary Gaussian type of Lamb vortex. In polar coordinates, the azimuthal and radial velocities  $u_\theta$  are given as

$$u_\theta = -re^{-ar^2}, \quad u_r = 0.$$

With the prescribed  $u_\theta$  and  $u_r$ , using the momentum and energy equations:

$$\frac{dp}{dr} = \frac{\rho u_\theta^2}{r} \quad (6.1)$$

$$\frac{\gamma}{(\gamma - 1)} \frac{p}{\rho} + \frac{u_\theta^2}{2} = H_0 \quad (6.2)$$

where  $H_0$  is a predescribed total enthalpy. By substituting (6.2) into (6.1), a differential equation for  $p$  is obtained and can be easily solved by numerical integration. Consequently,  $\rho$  and the entire stationary flow field is determined. The solution of this stationary vortex can then be superimposed to any uniform mean flow with a given streamwise velocity  $u_0$ . In the problem we consider,  $u_\theta$  and  $u_r$  are converted to:

$$u = \delta y e^{-ar^2}, \quad v = -\delta x e^{-ar^2},$$

where  $\delta = 0.3$  is a given amplitude factor, while  $p$  and  $\rho$ , as shown above, are functions of  $r$ , with

$$r^2 = ((x - u_0 t)^2 + y^2).$$

This stationary vortex is thus superimposed to the background mean flow. The vortex is large and strong, since the pressure in the vortex center dips down to about 7% of its circumferential value. Due to the presence of shocks, the CE/SE scheme is required to have enough numerical damping. For this purpose, a weighted average index  $\alpha = 2$  and numerical dissipation factor  $\epsilon = 0.5$  are chosen. The boundary conditions are the same as for the initial oblique shocks computation. We choose  $a = \frac{\ln 2}{784}$ ,  $\Delta t = 0.2$  and run 900 time steps. Fig. 6.10 demonstrates the interaction process at different time  $t=2, 20, 38, 56, 74, 92, 110, 128, 146$ , and 180. The vortex propagates downstream while remaining intact before colliding with the oblique shock. With further propagation, it begins to interact with the first oblique shock (Fig. 6.10 (2-3)). During the interaction, both vortex and shock are deformed or distorted. The straight oblique shock first changes to  $S$  shape and then recovers to its original straightline shape. At Stage 2, the collision disrupts the vortex. The ruptured vortex can no longer remain intact and begins to release its kinetic energy in the form of strong (non-linear) acoustic waves (pressure amplitude is as high as 17% of the field maximum). The phenomenon is consistent with others' experiments and numerical computations for a normal shock - vortex interaction. In Fig. 6.10 (3-4), the disrupted eddy continues to emit acoustic waves. Some of the waves pass through the reflected shock and are reflected from the solid wall. In Fig. 6.10 (5), the weakening vortex is flushed further down and collides with the second oblique shock. It is then further disrupted and releases more energy in the form of acoustic waves. At Stages 6, 7 and 8, more acoustic waves are emitted and the vortex reduces its size (to about 1/4 of its original size) and kinetic energy as well. In Fig. 6.10 (9-10), the vortex is flushed out from the computational domain along with the

acoustic waves it generates, and the oblique shocks resume their original shapes.

## 6.8 Acoustic Pulse / Shock-Wave Interaction

In order to demonstrate the capability of the CE/SE scheme to handle interactions of acoustic waves and shock waves, we describe an example of a weak acoustic pulse wave passing through a strong shock. We use a mesh of  $200 \times 200$  nodes. The domain is centered at the origin  $(0, 0)$ , with an extent of  $-100 \leq x \leq 100$  and  $-100 \leq y \leq 100$ . A steady oblique shock at a position along a diagonal of the computational domain is precalculated to form part of the initial condition for the computation. The initial conditions of an isolated acoustic pulse are superimposed on this precalculated shock to form the initial condition of the given problem. The data upstream and downstream of the shock are respectively

$$\begin{aligned} u_0 &= 2.378056, v_0 = 0, \\ p_0 &= 1 \text{ and } p_0 = 0.7142857; \end{aligned}$$

and

$$\begin{aligned} u_0 &= 2.1017481, v_0 = 0.4062729, \\ p_0 &= 1.5807555 \text{ and } p_0 = 1.3713613. \end{aligned}$$

A weak acoustic pulse propagating across a strong shock is considered. An acoustic pulse, initially centered at  $(x_0, y_0) = (-75, 0)$ , with initial data

$$u^* = v^* = 0, \quad p^* = \rho^* = \epsilon e^{-a[(x-x_0)^2+(y-y_0)^2]}$$

is superimposed on the mean flow, where the initial pulse amplitude  $\epsilon = 0.001$  and  $a = (\ln 2)/9$ . It is observed that the oblique shock strength is three orders of magnitude larger than the initial amplitude of the acoustic pulse. The pulse propagates in all directions with the speed of sound, while being carried downstream by the mean flow. During the computation, the non-reflecting boundary condition described above is enforced at all the four sides of the computational domain.

For such an interaction between a weak (linear) wave and a discontinuous wave, the theoretical exact solution is not available. However, the numerical results obtained with the CE/SE scheme demonstrate physically plausible phenomena. Fig. 6.11 illustrates the isobars at various time steps. At first, the acoustic pulse is blown downstream and propagates freely.

As the pulse collides with the strong oblique shock, the shock is practically unaffected, while the acoustic pulse ring is distorted in its passage through the shock, due to different speeds of sound and flow velocities on either side of the oblique shock.

In other examples described in [9], [15] and [16], the interactions of a strong (i.e. nonlinear) acoustic pulse, and of weak and strong vortical and entropy pulses with a strong shock were computed. Currently, the CE/SE method is being applied to benchmark problems in CAA and to supersonic jet noise computations, and has proved to be exceptionally accurate.

## 6.9 Three-Dimensional Inviscid Flow Examples

The CE/SE 3D Euler solver, which is an extension of the 1D Euler solver in the same way as is the 2D Euler solver, has recently been developed by X.Y. Wang and S.C. Chang. See Section 5 for the conceptual description of flux conservation using tetrahedrons in 3D. Details of the solver will be presented in a paper under preparation [?]. Some preliminary numerical results are presented in the following. In these results, a structured mesh of tetrahedrons is used, with  $\alpha = 1$  and  $\epsilon = 0.5$  in the entire domain.

(a) Oblique shock problem: To help with validation, the 3D Euler code is used to solve the 2D oblique shock reflection problem previously solved with the 2D Euler solver in [7]. The structured mesh consists of  $42 \times 14 \times 14 \times 6$  tetrahedral spatial cells in a domain  $0 \leq x \leq 4$ ,  $0 \leq y \leq 1$ , and  $0 \leq z \leq 1$ . The steady-state solution obtained with a time step  $\Delta t = 0.012$  is shown in Fig. 6.12, in which the density distribution in the entire domain and density contours at the plane  $y = 0$  are plotted.

(b) Flow past a ramp: For further validation, the 3D Euler code is used to solve a 2D supersonic flow of  $M_\infty = 2.2$  past a ramp with a compression angle  $\theta = 12^\circ$ , which has previously been solved using the 2D Euler solver in [22].  $40 \times 10 \times 10 \times 6$  tetrahedral cells are used in a domain  $-0.2 \leq x \leq 1.8$ ,  $0 \leq y \leq 1$ , and  $0 \leq z \leq 1$ , and a time step  $\Delta t = 0.005$  is used. The steady-state density distribution and density contours at the surface  $y = 0$  are shown in Fig. 6.13.

(c) Implosion/Explosion of a spherical shock wave in a cubical box.  $41 \times 41 \times 41 \times 6$  tetrahedral cells are

utilized in the computational domain specified by  $0 \leq x \leq 2$ ,  $0 \leq y \leq 2$ , and  $0 \leq z \leq 2$ . The symmetry inherent in the problem is utilized, so that the initial shock wave configuration is an eighth of a sphere, whose geometric center is at  $x = y = z = 0$  and whose radius is  $0.8\sqrt{3}$ . The interior of the sphere is a low pressure region with a pressure ratio of 10 across the shock. The density and pressure contour plots at different time levels obtained using a time step  $\Delta t = 0.005$  are shown in Fig. 6.14. The shock wave, contact surface, and expansion wave in Fig. 6.14 display physics similar to that seen in the 2-D implosion/explosion problem. More detailed description of the flow physics will be provided in [?].

## 7 Summary and Conclusions

In the present article, we reviewed the method of space-time conservation element and solution element (the CE/SE method, for short) for the numerical solution of conservation laws. We described several CE/SE schemes for computing fluid flows, and touched upon other CE/SE schemes and extensions. Our descriptions emphasized the geometry of the space-time discretization.

An ideal solver for smooth flows must be neutrally stable, explicit and two-level, and must be such that the discrete equations are invariant under space-time inversion. The CE/SE non-dissipative Euler solvers for isentropic flows meet all these requirements. In the present article, we described the non-dissipative 1D and 2D Euler solvers in terms of the conservation of piecewise linear space-time fluxes over discrete space-time volumes. Thus, given the space-time discretization, the schemes have a simple specification in terms of flux conservation. When shock waves are present in the solution, numerical dissipation must be introduced into numerical schemes in a controllable fashion, to model the irreversibility in the exact solution. We described the shock-capturing 1D Euler solver, which is a modification of the non-dissipative solver. The added numerical dissipation has a simple geometric description and a straightforward generalization to the 2D case. The Navier-Stokes solvers, not described here, reduce to the non-dissipative solvers when the physical viscosity vanishes, and hence the latter is never overwhelmed by numerical dissipation.

The key strategies that enable the CE/SE schemes to avoid the limitations of the upwind schemes are:

(i) The more general form of the conservation laws, i.e., the integral form, is cast in a form in which space and time are treated on an equal footing. This gives flexibility in the shape of the space-time conservation elements, which is useful for defining CEs when, for e.g., sources are present in the CE. (ii) A staggered space-time mesh is employed. This results in the simplest stencil. It also obviates the need for interpolation of fluxes at the interface between CEs. Thus, there is no need for an approximate Riemann solver. Hence, characteristics-based upwind-biasing methods, which are complicated and strictly valid only for smooth solutions, are avoided. There is thus also no compromise in the symmetry of treatment of the spatial fluxes. This also has implications for flows in multiple spatial dimensions. For the computation of such flows, upwind techniques must use directional splitting with its attendant difficulties. The CE/SE method in multiple spatial dimensions, on the other hand, does not involve any directional splitting. (iii) The flow property gradient is treated as an additional unknown in the CE/SE schemes. Therefore, there is no need for reconstruction of the flow gradient by polynomial curve fitting over neighboring mesh points, and for the subsequent use of complicated flux limiters. (iv) Space-time fluxes are conserved at both the local and global level. The condition of flux conservation, rather than any extrapolation, links the solution at a mesh point with its neighbors at the previous time level. This emphasis on the integral conservation law is critical for accurate flow simulations, particularly if they involve long marching times and/or regions of rapid change (e.g., boundary layers and shocks).

We reproduced here several numerical results obtained with various CE/SE flow solvers. The results included a demonstration of extremely simple yet highly effective non-reflecting boundary conditions for the extended Sod's shock-tube problem. The CE/SE solver for the scalar convection-diffusion equation was shown to be accurate in all Reynolds number regimes. The CE/SE solver for the 1D and 2D Euler equations with source terms simulating detonation was also shown. We reproduced numerical solutions obtained with the 2D CE/SE Euler solver, including the process of diffraction of a shock wave around a wedge and the implosion/explosion of a polygonal shock wave in a box, as well as computational aeroacoustic phenomena involving the interaction of strong shocks and weak acoustics as well as strong shocks and strong vortices. The results reproduced here are only some of the difficult problems readily solved with CE/SE schemes; see [1-31]

for more examples.

We remark here that the CE/SE schemes developed thus far are characterized by simplicity, generality of applicability and second-order accuracy in space and time. The simplest possible stencils are employed. The 2D spatial mesh is constructed from triangles, and the 3D spatial mesh will be constructed from tetrahedra. Triangles and tetrahedra are the simplest polytopes in 2D and 3D, respectively. The 1D and 2D Euler solvers bear a remarkable resemblance to the solvers of the 1D and 2D scalar convection-diffusion equations, respectively, with the discrete equations in the former two being matrix versions of the scalar equations in the latter two. All of the above schemes are characterized by virtually the same properties. Furthermore, the viscous flow solvers are designed to reduce to the respective non-dissipative solvers when the physical viscosity vanishes. The CE/SE method thus represents a new unified framework for the numerical solution of conservation laws.

## Acknowledgement

The authors would like to thank Dr. H.T. Huynh of NASA Lewis Research Center for valuable discussions regarding upwind and centered schemes.

## References

- [1] S.C. Chang and W.M. To, "A New Numerical Framework for Solving Conservation Laws – The Method of Space-Time Conservation Element and Solution Element", NASA TM 104495, August 1991.
- [2] S.C. Chang, "On an Origin of Numerical Diffusion: Violation of Invariance Under Space-Time Inversion", *Proceedings of the 23rd Modeling and Simulation Conference*, April 30 - May 1, 1992, Pittsburgh, PA, William G. Vogt and Marlin H. Mickle eds., Part 5, pp. 2727-2738. Also published as NASA TM 105776.
- [3] S.C. Chang and W.M. To, "A Brief Description of a New Numerical Framework for Solv-

- ing Conservation Laws – The Method of Space-Time Conservation Element and Solution Element”, *Proceedings of the 13th International Conference on Numerical Methods in Fluid Dynamics*, July 6-10, 1992, Rome, Italy, M. Napolitano and F. Sabetta, eds., Lecture Notes in Physics 414, Springer-Verlag, pp. 396-400. Also published as NASA TM 105757.
- [4] S.C. Chang, “New Developments in the Method of Space-Time Conservation Element and Solution Element – Applications to the Euler and Navier-Stokes Equations”, presented at the Second U.S. National Congress on Computational Mechanics, August 16-18, 1993, Washington D.C. Published as NASA TM 106226.
- [5] S.C. Chang, X.Y. Wang and C.Y. Chow, “New Developments in the Method of Space-Time Conservation Element and Solution Element – Applications to Two-Dimensional Time-Marching Problems”, NASA TM 106758, December 1994.
- [6] S.C. Chang, “The Method of Space-Time Conservation Element and Solution Element – A New Approach for Solving the Navier-Stokes and Euler Equations”, *J. Comput. Phys.*, **119** pp. 295-324, (1995).
- [7] S.C. Chang, X.Y. Wang and C.Y. Chow, “The Method of Space-Time Conservation Element and Solution Element – Applications to One-Dimensional and Two-Dimensional Time-Marching Flow Problems”, AIAA Paper 95-1754-CP, in *A Collection of Technical Papers, 12th AIAA CFD Conference*, June 19-22, 1995, San Diego, CA, pp. 1258-1291. Also published as NASA TM 106915.
- [8] S.C. Chang, X.Y. Wang, C.Y. Chow and A. Himansu, “The Method of Space-Time Conservation Element and Solution Element – Development of a New Implicit Solver”, *Proceedings of the Ninth International Conference on Numerical Methods in Laminar and Turbulent Flow*, July 10-14, 1995, Atlanta, GA, C. Taylor and P. Durbetaki, eds., Volume IX, Part I, Pineridge Press, pp. 82-93. Also published as NASA TM 106897.
- [9] S.C. Chang, C.Y. Loh and S.T. Yu, “Computational Aeroacoustics via a New Global Conservation Scheme”, *Proceedings of the 15th International Conference on Numerical Methods in Fluid Dynamics*, P.Kutler, J. Flores and J.-J. Chattot, eds., June 24-28, 1996, Monterey, CA.
- [10] S.C. Chang and A. Himansu, “The Implicit and Explicit  $a\text{-}\mu$  Schemes”, NASA TM 97-206307, November 1997.
- [11] S.C. Chang, S.T. Yu, A. Himansu, X.Y. Wang, C.Y. Chow and C.Y. Loh, “The Method of Space-Time Conservation Element and Solution Element – A New Paradigm for Numerical Solution of Conservation Laws”, to appear in *Computational Fluid Dynamics Review 1997*, M.M. Hafez and K. Oshima, eds., John Wiley and Sons, West Sussex, UK.
- [12] S.C. Chang, A. Himansu, C.Y. Loh, X.Y. Wang, S.T. Yu and P.C.E. Jorgenson, “Robust and Simple Non-Reflecting Boundary Conditions for the Space-Time Conservation Element and Solution Element Method”, AIAA Paper 97-2077, presented at the 13th AIAA CFD Conference, June 29-July 2, 1997, Snowmass, CO.
- [13] C.Y. Loh, S.C. Chang, J.R. Scott and S.T. Yu, “Application of the Method of Space-Time Conservation Element and Solution Element to Aeroacoustics Problems”, *A Collection of Technical Papers, Volume II*, pp. 713-718, 6th International Symposium on Computational Fluid Dynamics, September 4-8, 1995, Lake Tahoe, NV.
- [14] C.Y. Loh, S.C. Chang, J.R. Scott and S.T. Yu, “The Space-Time Conservation Element Method – A New Numerical Scheme for Computational Aeroacoustics”, AIAA Paper 96-0276, presented at the 34th AIAA Aerospace Sciences Meeting, January 15-18, 1996, Reno, NV.
- [15] C.Y. Loh, S.C. Chang and J.R. Scott, “Computational Aeroacoustics via the Space-Time Conservation Element / Solution Element Method”, AIAA Paper 96-1687, presented at the 2nd AIAA/CEAS Aeroacoustics Conference, May 6-8, 1996, State College, PA.
- [16] C.Y. Loh, L.S. Hultgren and S.C. Chang, “Computing Waves in Compressible Flow Using the Space-Time Conservation Element and Solution Element method”, AIAA Paper 98-0369, presented at the 36th AIAA Aerospace Sciences Meeting, January 12-15, 1998, Reno, NV.
- [17] S.J. Park, S.T. Yu., M.C. Lai, S.C. Chang and P.C.E. Jorgenson, “Direct Calculations of Stable and Unstable ZND Detonations by the Space-Time Conservation Element and Solution

- Element Method," AIAA paper 98-3212, presented at 34th AIAA/ASME/SAE/ASEE Joint Propulsion Conference & Exhibit, July 13-15, 1998, Cleveland, OH.
- [18] S.T. Yu and S.C. Chang, "Treatments of Stiff Source Terms in Conservation Laws by the Method of Space-Time Conservation Element and Solution Element", AIAA Paper 97-0435, presented at the 35th AIAA Aerospace Sciences Meeting, January 6-10, 1997, Reno, NV.
- [19] S.T. Yu and S.C. Chang, "Applications of the Space-Time Conservation Element / Solution Element Method to Unsteady Chemically Reactive Flows", AIAA Paper 97-2099, in *A Collection of Technical Papers, 13th AIAA CFD Conference*, June 29-July 2, 1997, Snowmass, CO.
- [20] S.T. Yu, S.C. Chang, P.C.E. Jorgenson, S.J. Park and M.C. Lai, "Treating Stiff Source Terms in Conservation Laws by the Space-Time Conservation Element and Solution Element Method," To appear in the *Proceedings of the 16th International Conference on Numerical Method in Fluid Dynamics*, Arcachon, France, July 6-July 10, 1998.
- [21] X.Y. Wang, C.Y. Chow and S.C. Chang, "Application of the Space-Time Conservation Element and Solution Element Method to Shock-Tube Problem", NASA TM 106806, December 1994.
- [22] X.Y. Wang, "Computational Fluid Dynamics Based on the Method of Space-Time Conservation Element and Solution Element", Ph.D. Dissertation, 1995, Department of Aerospace Engineering, University of Colorado, Boulder, CO.
- [23] X.Y. Wang, C.Y. Chow and S.C. Chang, "Application of the Space-Time Conservation Element and Solution Element Method to Two-Dimensional Advection-Diffusion Problems", NASA TM 106946, June 1995.
- [24] X.Y. Wang, S.C. Chang and C.Y. Chow, "Application of the Method of Space-Time Conservation Element and Solution Element to Axisymmetric Euler Time-Marching Problems," *A Collection of Technical Papers, Volume III, pp. 1351-1356, 6th International Symposium on Computational Fluid Dynamics*, September 4-8, 1995, Lake Tahoe, Nevada.
- [25] X.Y. Wang, C.Y. Chow and S.C. Chang, "High Resolution Euler Solvers Based on the Space-Time Conservation Element and Solution Element Method", AIAA Paper 96-0764, presented at the 34th AIAA Aerospace Sciences Meeting, January 15-18, 1996, Reno, NV.
- [26] X.Y. Wang, C.Y. Chow and S.C. Chang, "Numerical Simulation of Flows Caused by Shock-Body Interaction", AIAA Paper 96-2004, presented at the 27th AIAA Fluid Dynamics Conference, June 17-20, 1996, New Orleans, LA.
- [27] X.Y. Wang, C.Y. Chow and S.C. Chang, "An Euler Solver Based on the Method of Space-Time Conservation Element and Solution Element", *Proceedings of the 15th International Conference on Numerical Methods in Fluid Dynamics*, P.Kutler, J. Flores and J.-J. Chattot, eds., June 24-28, 1996, Monterey, CA.
- [28] X.Y. Wang, C.Y. Chow and S.C. Chang, "Numerical Simulation of Gust Generated Aeroacoustics in a Cascade Using the Space-Time Conservation Element and Solution Element Method," AIAA Paper 98-0178, presented at the 36th AIAA Aerospace Sciences Meeting, January 12-15, 1998, Reno, NV.
- [29] X.Y. Wang, C.Y. Chow and S.C. Chang, "Numerical Simulation of Shock Reflection over a Dust Layer Model Using the Space-Time Conservation Element and Solution Element Method," AIAA Paper 98-0443, presented at the 36th AIAA Aerospace Sciences Meeting, January 12-15, 1998, Reno, NV.
- [30] X.Y. Wang, C.Y. Chow and S.C. Chang, "Non-reflecting Boundary Conditions Based on the Space-Time CE/SE Method for Free Shear Flows," AIAA paper 98-3020, presented at the 29th AIAA Fluid Dynamics Conference, Albuquerque, New Mexico, June 15-18, 1998.
- [31] X.Y. Wang, S.C. Chang, K.H. Kao, and P.C.E. Jorgenson, "A Non-Splitting Unstructured-Triangular-Mesh Euler Solver Based on the Method of Space-Time Conservation Element and Solution Element," to appear in the *Proceedings of the 16th International Conference on Numerical Method in Fluid Dynamics*, Arcachon, France, July 6-July 10, 1998.
- [32] X.Y. Wang and S.C. Chang, "A Three-Dimensional Unstructured Euler Solver Based on the Space-Time Conservation Element and

- Solution Element Method," NASA Technical Memorandum, in preparation.
- [33] P. Batten, M.A. Leschziner and U.C. Goldberg, "Average-State Jacobians and Implicit Methods for Compressible Viscous and Turbulent Flows," *J. Comp. Phys.* **137**, 38 (1997).
  - [34] T. Molls and F. Molls, "Space-Time Conservation Method Applied to Saint Venant Equation," *Journal of Hydraulic Engineering*, **124**, p. 501 (1998)
  - [35] Z. Zhang and M. Shen, "New Approach to Obtain Space-Time Conservation Schemes," *Chinese J. of Aeronautics*, **10**(3), p. 87 (1997).
  - [36] Z. Zhang and M. Shen, "Improved Scheme of Space-Time Conservation Element and Solution Element," *J. of Tsinghua University (Sci & Tech)*, **37**(8), p. 65 (1997).
  - [37] Z. Zhang, M. Shen and H. Li, "Modified Space-Time Conservation Schemes for 2D Euler Equations," presented at the 7th International Symposium on Computational Fluid Dynamics, September 1997, Beijing, China.
  - [38] Z. Zhang, H. Li and M. Shen, "Space-Time Conservation Scheme for 3D Euler Equations," presented at the 7th International Symposium on Computational Fluid Dynamics, September 1997, Beijing, China.
  - [39] Z. Zhang, "A New General Space-Time Conservation Scheme for 2D Euler Equations," *Chinese J. of Computational Mechanics*, **14**(4), p. 377 (1997).
  - [40] B. van Leer, *J. Comput. Phys.*, **23** (1977), pp. 263-275.
  - [41] B. van Leer, *J. Comput. Phys.*, **23** (1977), pp. 276-299.
  - [42] H.T. Huynh, *SIAM J. Numer. Anal.*, **32**, 5 (1995), pp. 1565-1619.
  - [43] P. Lax, "Hyperbolic Systems of Conservation Laws and the Mathematical Theory of Shock Waves," *SIAM*, Philadelphia, Pennsylvania (1973).
  - [44] A. Harten, *J. Comput. Phys.*, Vol. 49 (1983), pp. 357-393.
  - [45] A. Harten, B. Engquist, S. Osher, and S. Chakravarthy, *J. Comput. Phys.*, Vol. 71 (1987), pp. 231-303.
  - [46] P.L. Roe, *Ann. Rev. Fluid Mech.*, Vol. 18 (1986), pp. 337-365.
  - [47] H. Nessyahu and E. Tadmor, "Non-oscillatory central differencing for hyperbolic conservation laws", *J. Comp. Phys.*, **87** (1990), pp. 408-463.
  - [48] R. Sanders, "A third-order accurate variation nonexpansive difference scheme for single nonlinear conservation laws", *Math. Comp.*, **51** (1988), pp. 535-558.
  - [49] R. Sanders and A. Weiser, "A high order staggered grid method for hyperbolic systems of conservation laws in one space dimension", *Computer Methods in Applied Mechanics and Engineering*, **75** (1989), pp. 91-107.
  - [50] R. Sanders and A. Weiser, "A high resolution staggered-mesh approach for nonlinear hyperbolic systems of conservation laws", *J. Comp. Phys.*, **101** (1992), pp. 314-329.
  - [51] G.D. van Albada, B. van Leer, and W.W. Roberts, *Astronom. Astrophys.*, Vol. 108 (1982), p.76.
  - [52] G.A. Sod, *J. Comput. Phys.*, Vol. 27 (1978), pp. 1-31.
  - [53] G.D. Smith, *Numerical Solution of Partial Differential Equations: Finite Difference Methods*, 3rd ed., 1985. Oxford Univ. Press, New York.
  - [54] W. Fickett and W.W. Wood, "Flow Calculations for Pulsating One-Dimensional Detonations," *Physics of Fluids*, **9**(3) (1966) pp . 903-916.
  - [55] H. Oertel, Sr., 1966 *Stossrohre*, Vienna: Springer-Verlag.
  - [56] T. Aki and F. Higashino, AIP Conference Proceedings 208, 1989.
  - [57] S.T. Yu, Y.-L.P. Tsai and K.C. Hsieh, "Simulating Waves in Flows by Runge-Kutta and Compact Difference Schemes", AIAA Journal, Vol. **33**, No. 3, pp. 421-429. Also presented as AIAA Paper 92-3210.

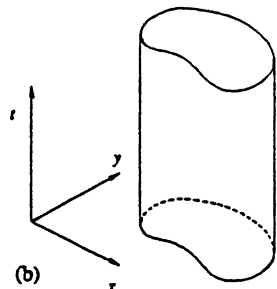
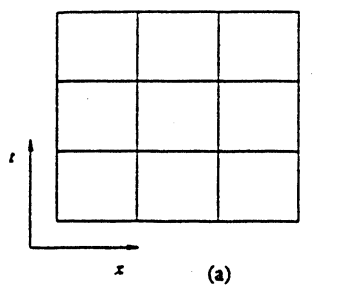


Figure 2.1 — Space-time conservation elements for methods using a fixed spatial domain: (a) one space dimension (b) two space dimensions

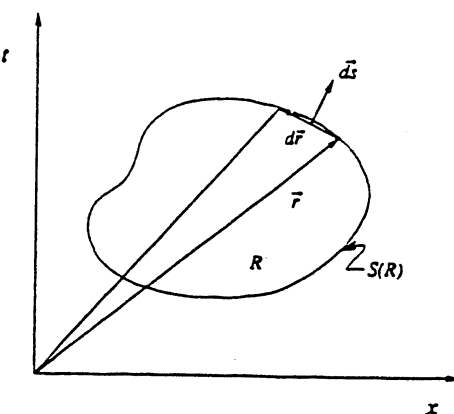


Figure 2.2 — A space-time conservation element with an arbitrary space-time domain

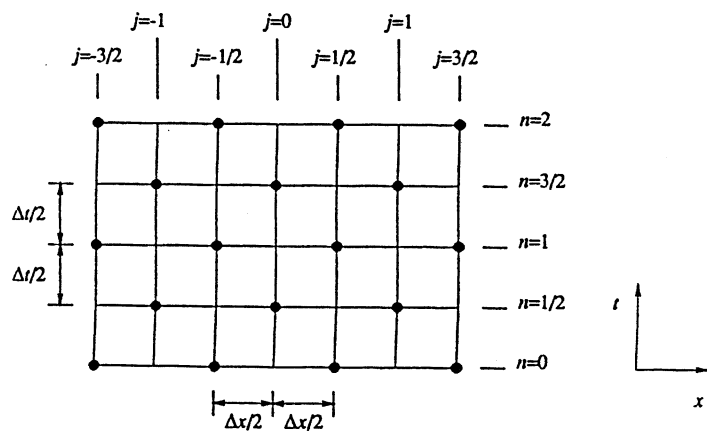


Figure 3.1 — The space-time mesh

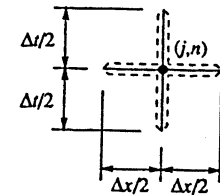


Figure 3.2 —  $SE(j,n)$

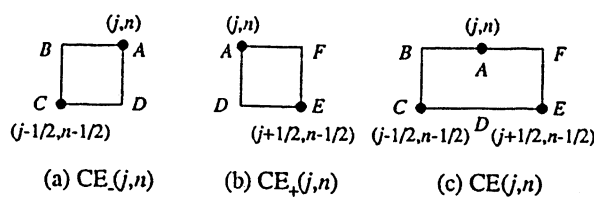


Figure 3.3 — The CEs associated with the mesh point  $(j,n)$

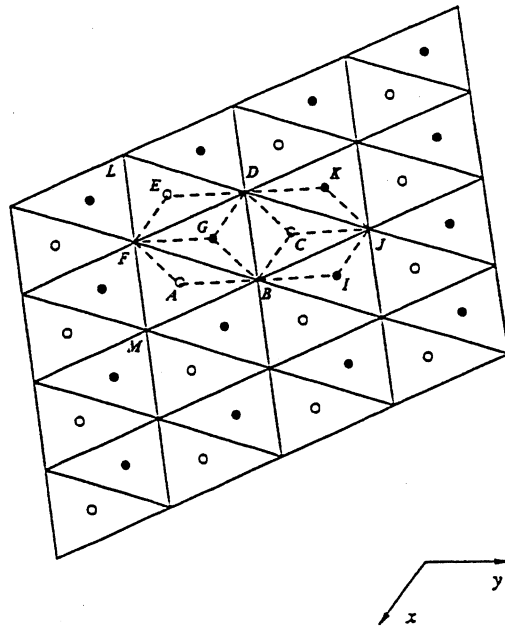


Figure 4.1 — A spatial domain formed from congruent triangles,  
showing the spatial projections of the mesh points

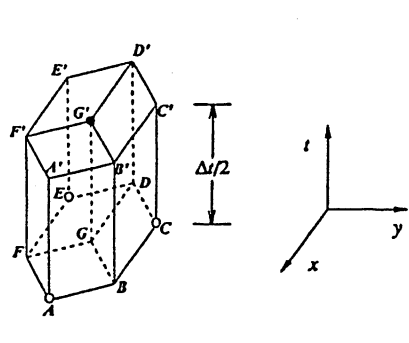


Figure 4.2 — The CEs associated with  $G'$

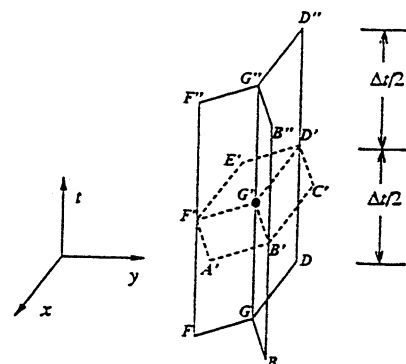


Figure 4.3 — The SE associated with the point  $G'$

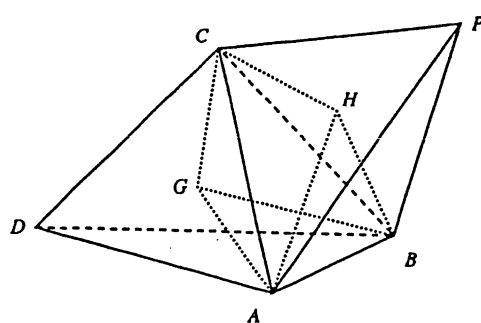


Figure 5.1 — Spatial projection of part of a 3D space-time mesh,  
showing the construction of a CE

Fig. 6.1 The CE/SE solution of the extended Sod's problem at  $t=0$

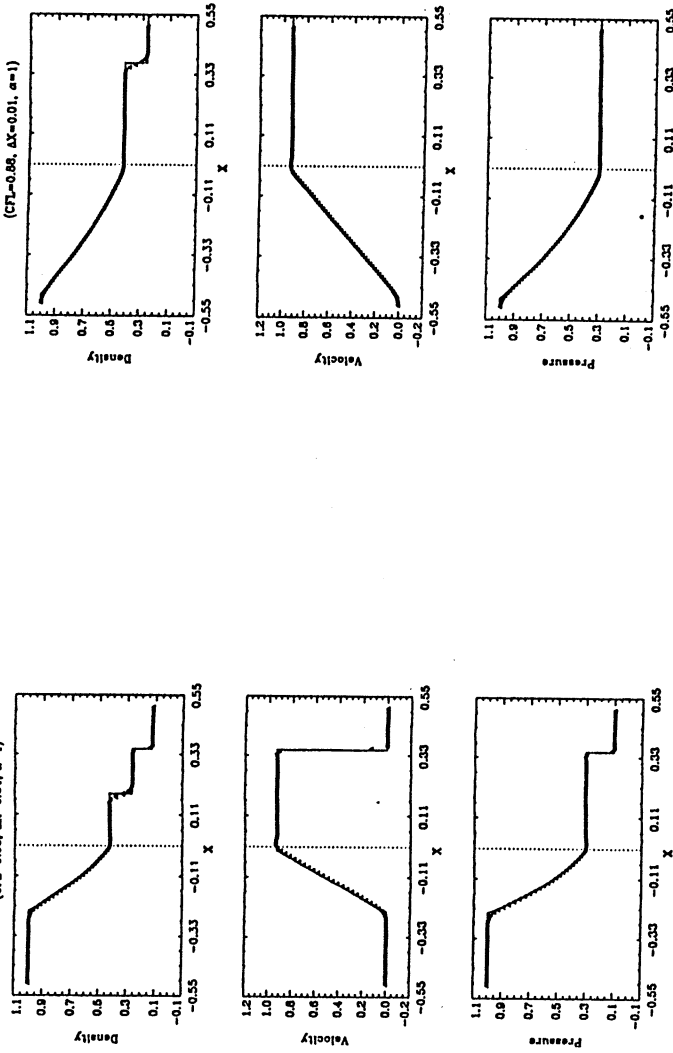


Fig. 6.2 The CE/SE solution of the extended Sod's problem at  $t=0.4$

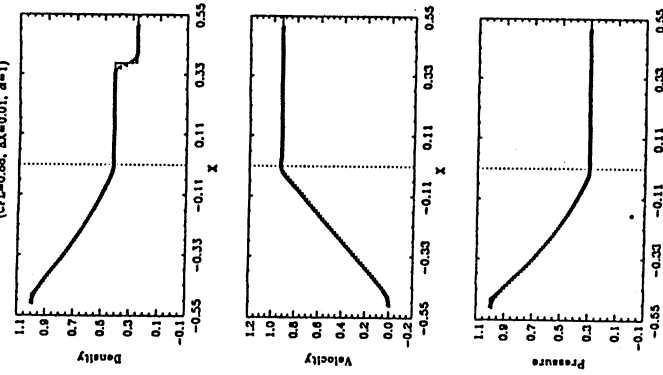


Fig. 6.3 The CE/SE solution of the extended Sod's problem at  $t=0.6$

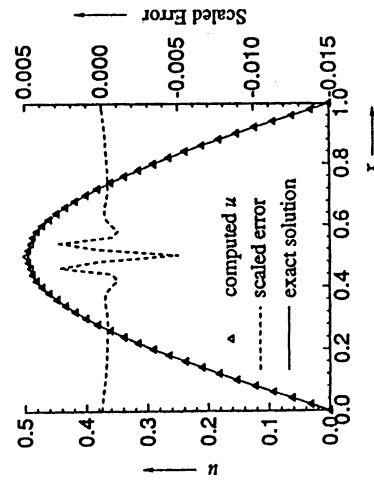
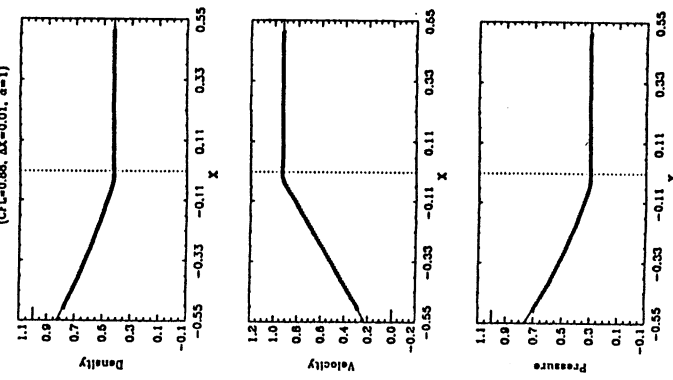


Figure 6.4 — Implicit  $\alpha\text{-}\mu$  Scheme : Pure Diffusion

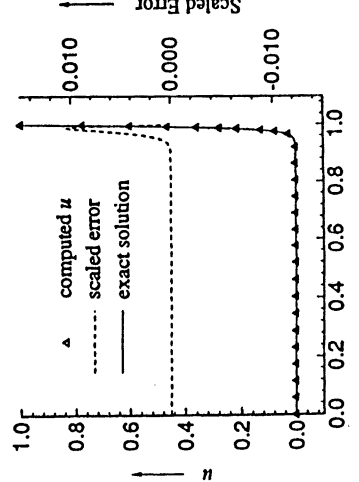


Figure 6.5 — Implicit  $\alpha\text{-}\mu$  Scheme : Boundary Layer,  $Re = 100$

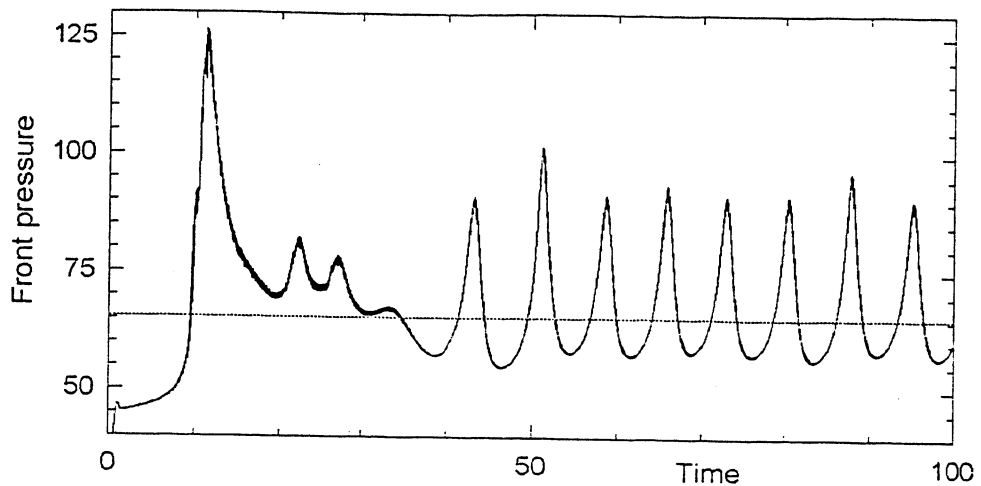


Fig. 6.6 (a) — Front Pressure of Unstable 1D ZND Detonation Wave

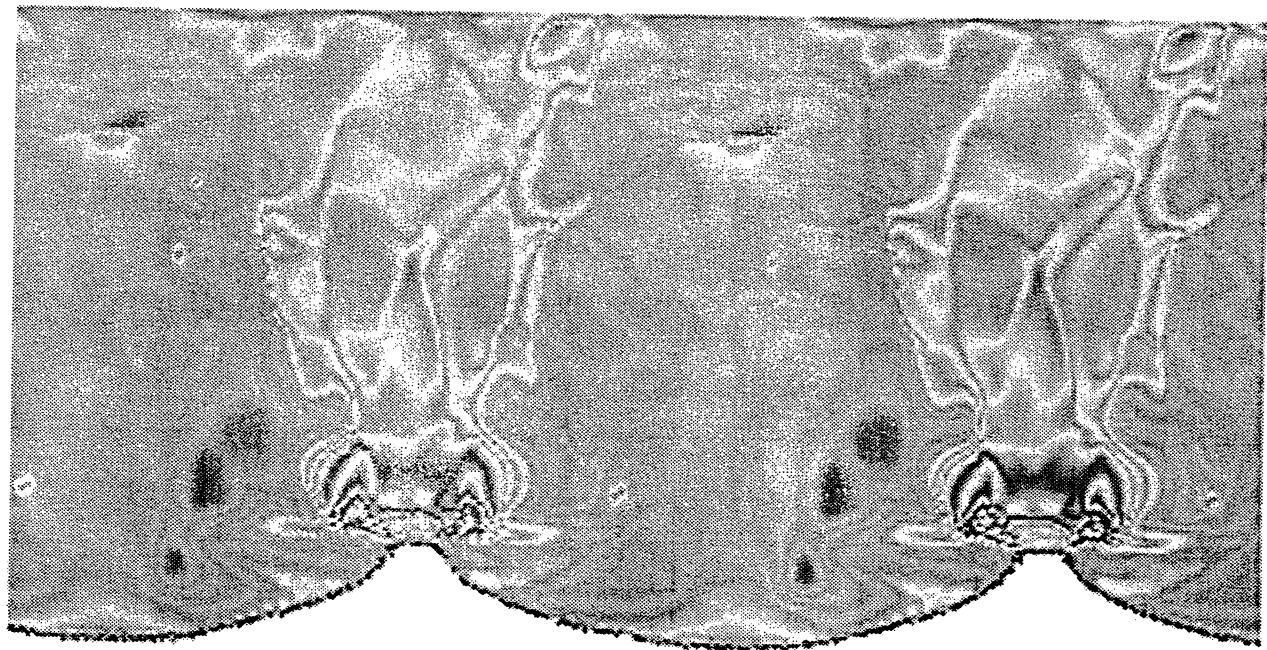


Fig. 6.6 (b) — Pressure Contours of Unstable 2D ZND Detonation Wave

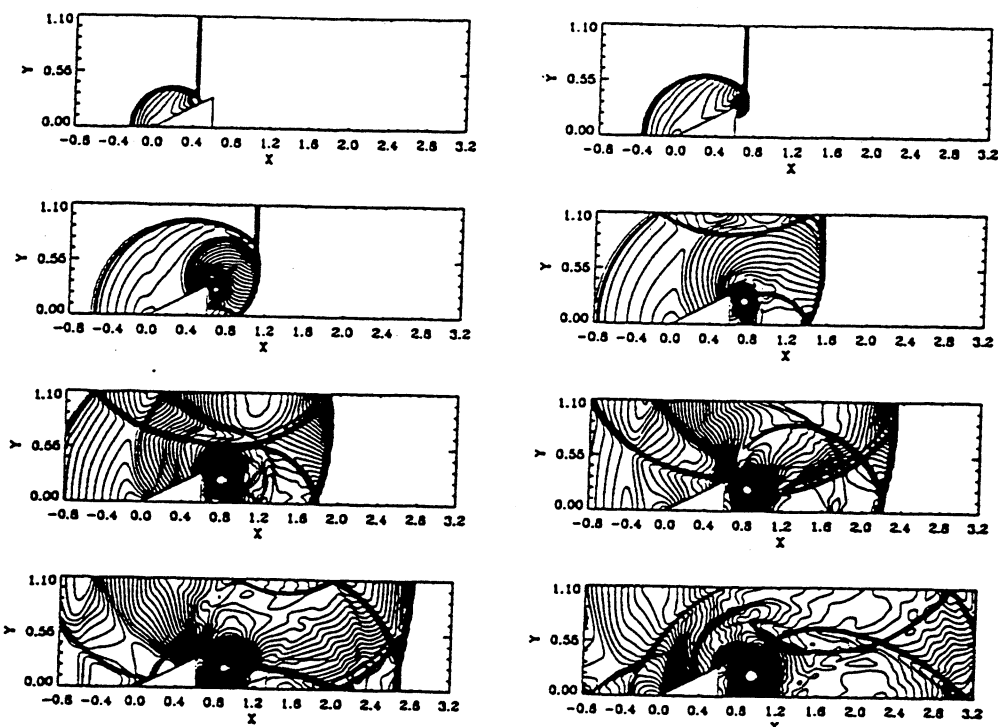


Fig. 6.7 Diffraction of a shock wave around a wedge:  
Density contours of the CE/SE solution

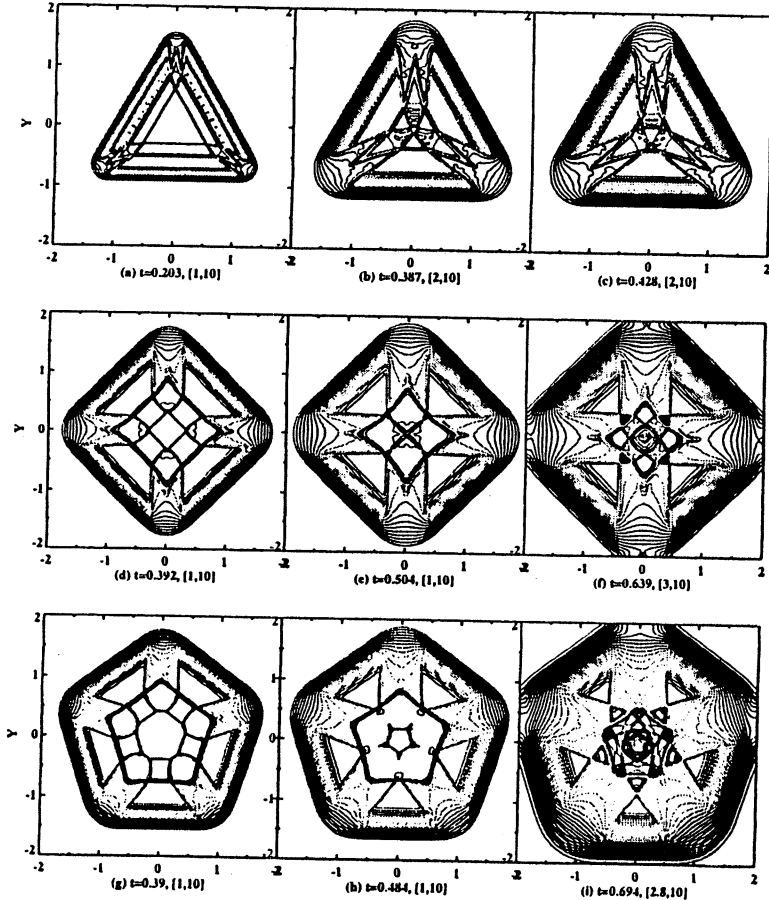


Fig. 6.8 Density contours for implosion/explosion of a polygonal shock in a square box

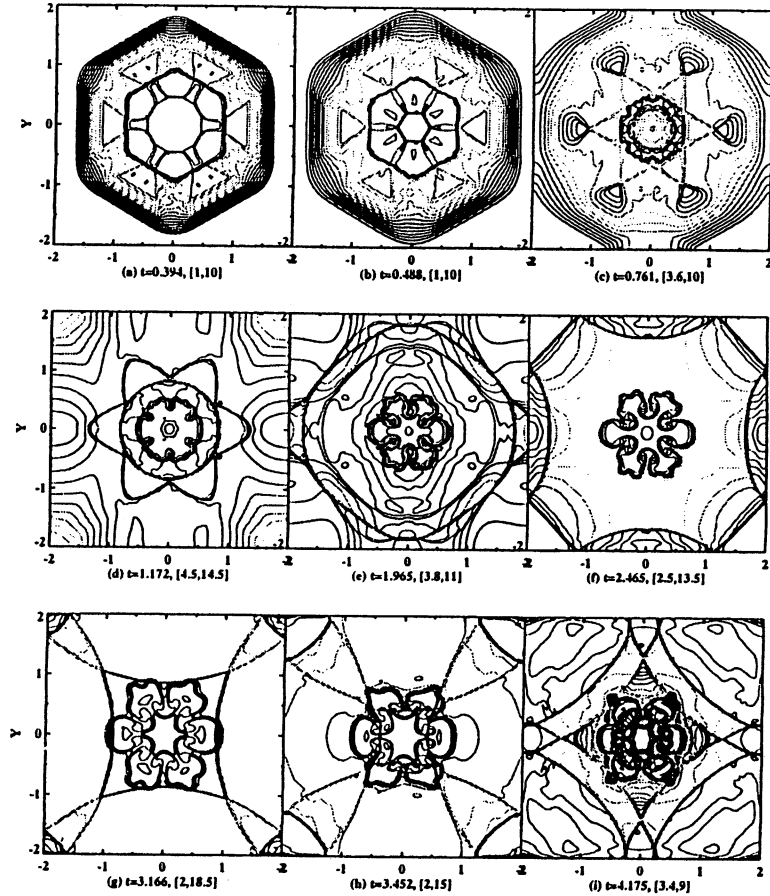
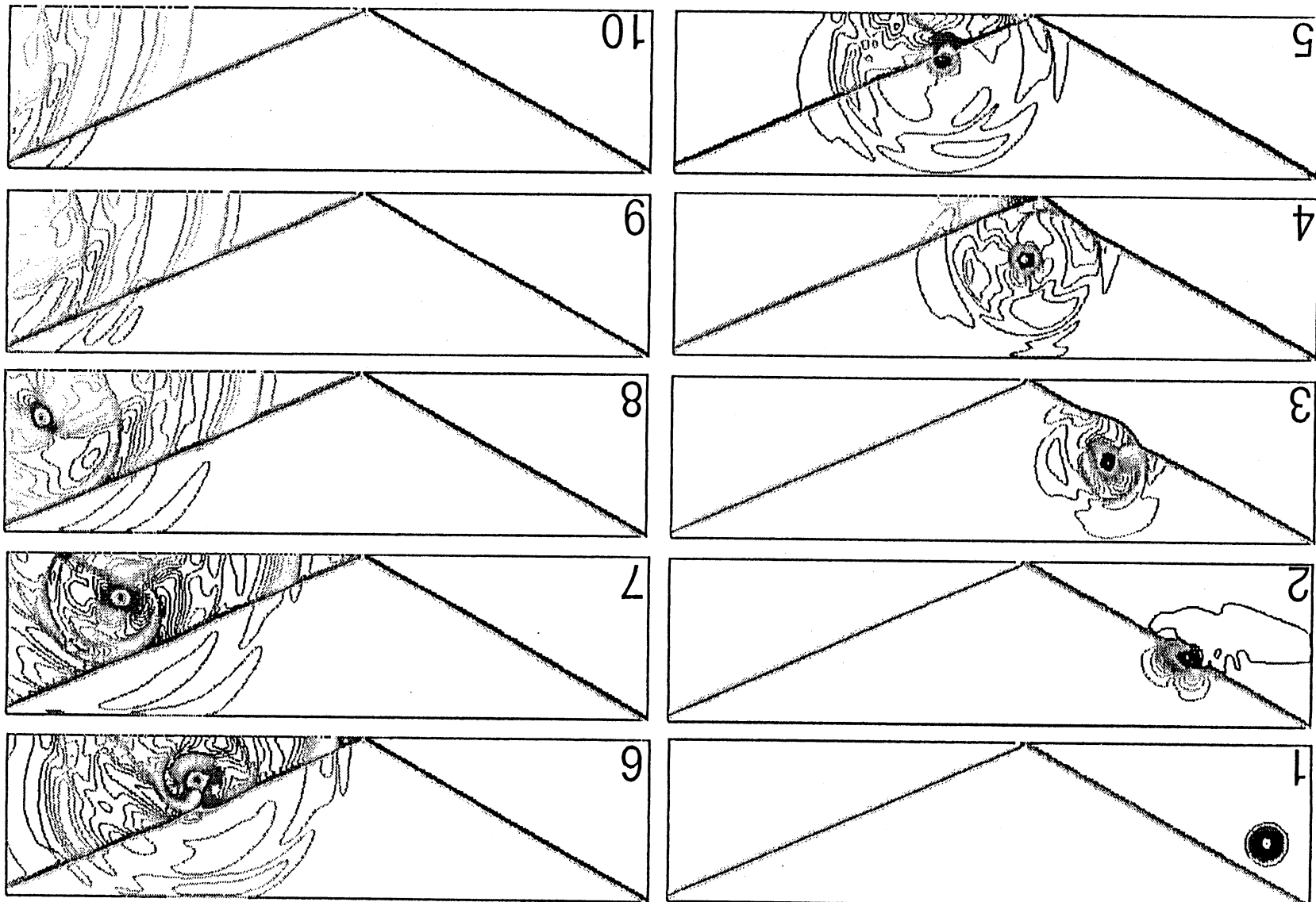


Fig. 6.9 Density contours for implosion/explosion of a hexagonal shock in a square box

acoustic waves generated.

Figure 6.10 isobars for a vortex passing through shocks, with



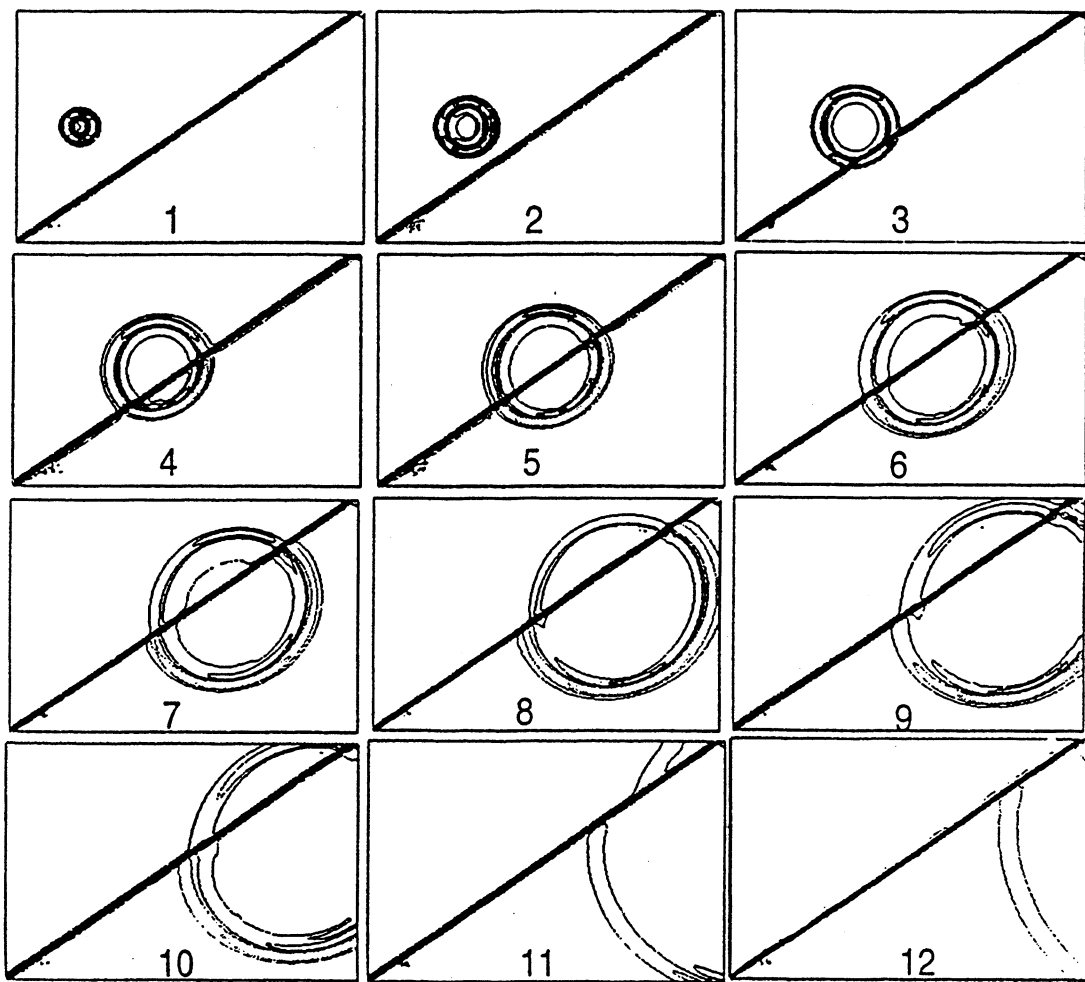


Fig. 6.11 Isobars for interaction of an acoustic pulse with a shock wave

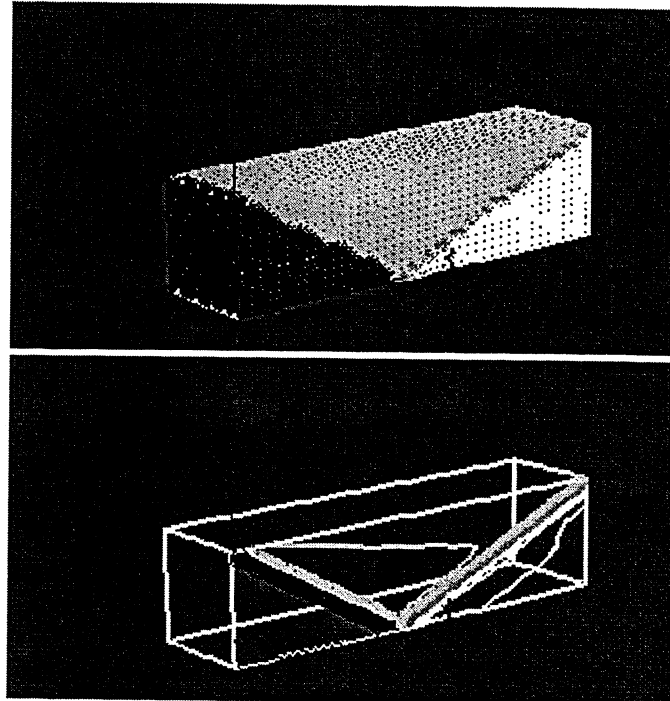


Figure 6.12 The oblique shock problem.

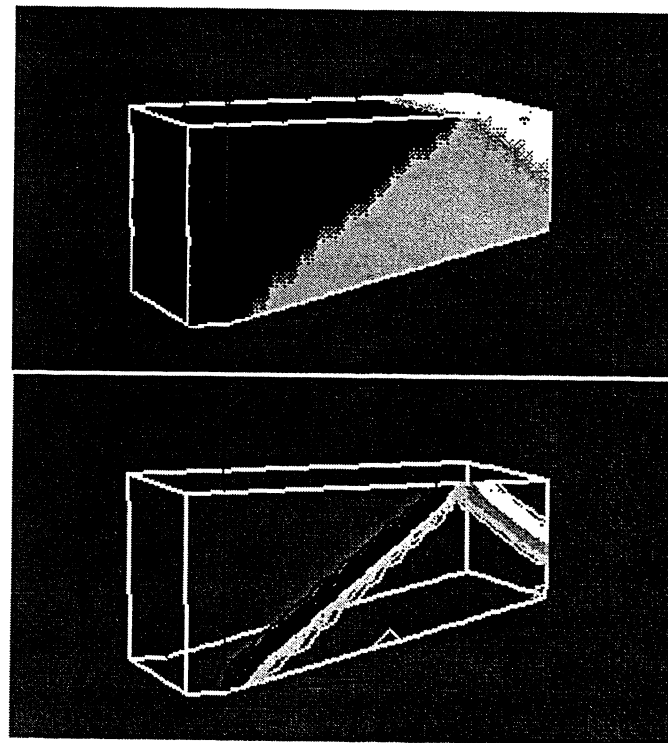


Figure 6.13 Flow past a 3-D ramp.

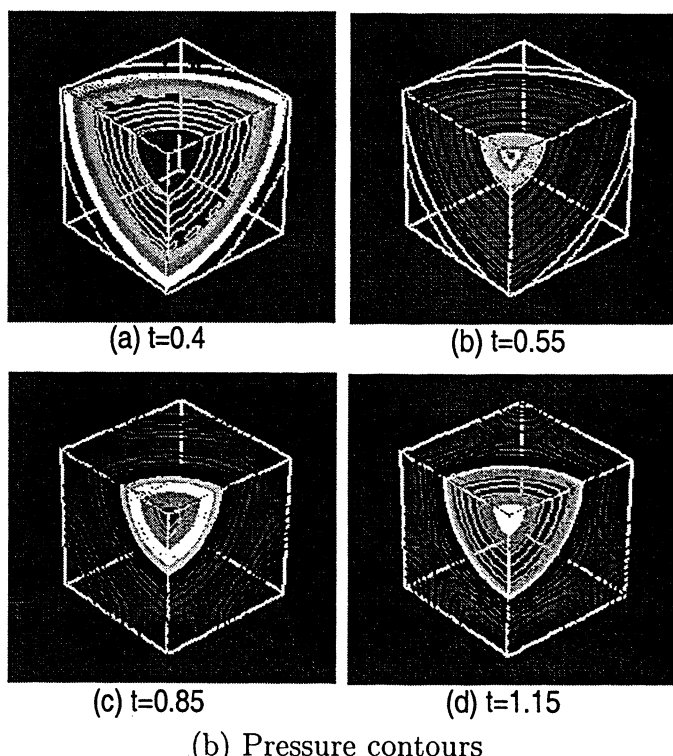
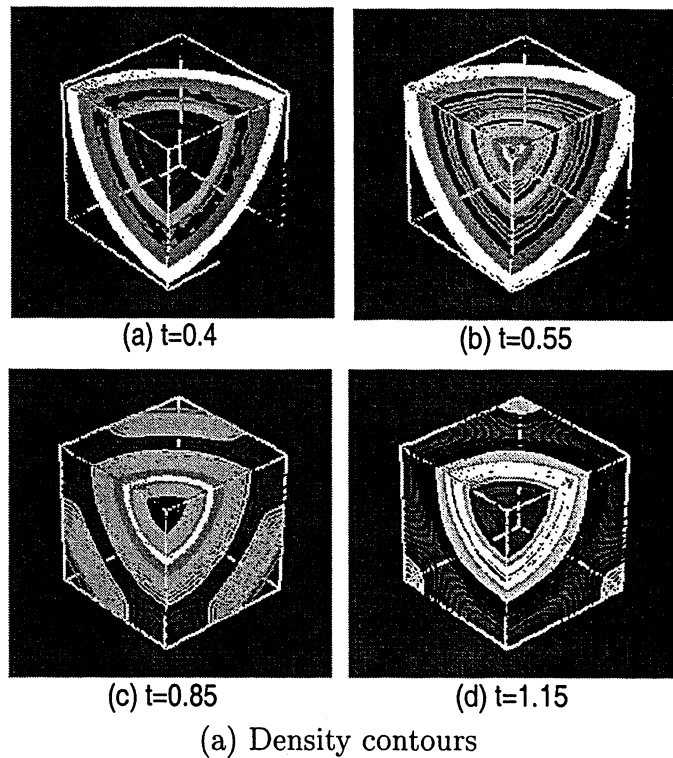


Figure 6.14 Implosion/explosion of a spherical shock wave at different time levels.

